Analysis of muon events with tau double bang reconstruction Belle Starr

Bachelorarbeit aus der Physik

vorgelegt von
Nico Baßler
16. 12. 2016

Erlangen Centre for Astroparticle Physics
Friedrich-Alexander-Universität Erlangen-Nürnberg

Betreuer: Prof. Dr. Uli Katz

Abstract

Neutrino telescopes use the reconstruction of muon tracks to resolve astronomical objects. Neutrino astronomy is a promising method for solving many astronomical and fundamental physics problems such as the classification of dark matter. The KM3NeT neutrino telescope uses a detector layout completely different from any existing detector layout. Thus, the track reconstruction has to be reimplemented.

This work concentrates on the energy loss reconstruction. The starting point for this is the tau double bang reconstruction Belle Starr, which I modify to be applicable to muons.

The muon data used to test the quality of all reconstructions performed is simulated in a Monte Carlo (MC) chain. The quality of every reconstruction step implemented or considered for implementation is discussed. Then reconstructed parameters are investigated in order to place cuts on the data to ensure that the part of the dataset used for further analysis is well reconstructed. This well reconstructed data is further analyzed to estimate the quality of the reconstructions for different implementations and parameters. This reconstruction of energy losses along a muon track is then used to differentiate muon bundles from muons due to neutrino interactions.

Both the position and energy reconstruction have problems. The position is reconstructed well for about half of the data. Similar reconstructed likelihoods yield energies with different orders of magnitude making it impossible to properly correlate them. The classification of muon events is worse (7 % error) than by other parameters already used by the collaboration (1 % error) due to this large error.

The method represented is a way to reconstruct vertex positions, but it has to be further refined for this specific application. The energy can not be reconstructed with the method discussed here and it has to be implemented separately. If this is done, the characterization methods discussed should be reviewed, but they should not be used due to the high error rate at the moment.

Contents

1 Introduction

KM3NeT is the name of a large scale international experiment. It is a deep-sea neutrino telescope. Currently KM3NeT is in the phase of having the first detector lines connected to the experiment. It is divided into two experiments with different purposes. The experiment of interest for this thesis is ARCA (**A**stroparticle **R**esearch with **C**osmics in the **A**byss). It is the larger part of the experiment and intended to record high energy neutrinos in order to resolve distant astronomical objects of interest like active galactic centers, starburst galaxies and supernova remnants. Neutrino astronomy is crucial for our understanding of many physical models. Examples for the usage of neutrino astronomy are studies about the origin of cosmic rays and examination of models for the origins and properties of dark matter.

In the scope of such a large experiment, the collaboration has to run simulations. Simulations are used to determine parameters which can not be calculated analytically and to prepare the software for use on real data. They are also used to determine the efficiency of the algorithms in development.
Most detected particles are muons. There are two major muon sources: Atmospheric showers and neutrino interactions in water. A study of these muons amounts to a study of the neutrinos which produced them or the cosmic rays which produced them.

There is currently no reconstruction for cascades along track-like events, which is needed to resolve the energy loss structure of high-energy muons. A reconstruction for tau double bang events exists. Since tau double bang events usually are two successive showers, the reconstruction deals with multiple energy losses. The plan is to rewrite this reconstruction, Belle Starr, in order to be applicable to muon event files. Then an analysis of said reconstruction is performed to gauge its usefulness. All data analysis is done on simulated files since the detector has not been completely built yet.

KM3NeT is not the first neutrino telescope in the deep sea. Its philosophical predecessors are ANTARES and IceCube. KM3NeT is larger than both of these experiments. It also has different optical modules with a much higher angular resolution. Since the technical details of the optical modules are so different, reconstruction algorithms from ANTARES and IceCube can not simply be reused for KM3NeT without modifying them.

2 Experimental setup

A rough overview of the geometry of the ARCA experiment will be useful in understanding the latter part of this thesis. If the reader has already read the letter of intent for the KM3NeT experiment [Adr16], this will only be a refresher.

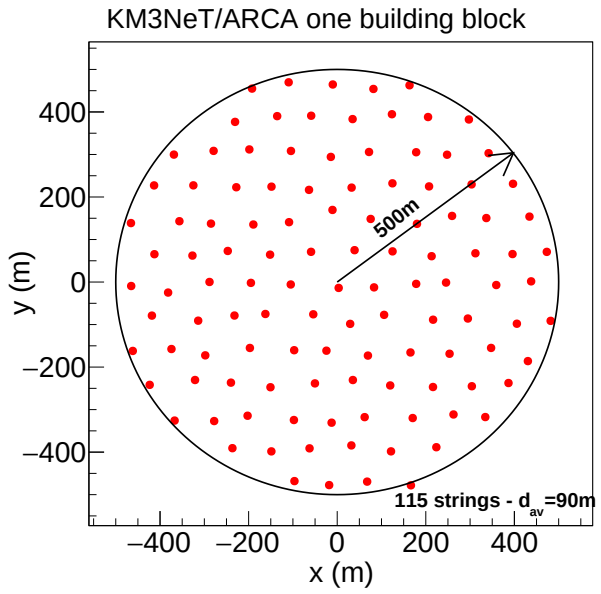

Figure 2.1: *Positions of strings in the ARCA detector. The red dots indicate detection string under water. Taken from [Adr16](Figure 15)*

The current plans (see Figure 2.1) for the ARCA detector imply its geometry in the simulations. The following description is not of the detector itself, but the layout of one detector module assumed in simulations. There are two definitions of the detector. One is the actual detection volume, the other the detection volume with some buffer for simulation purposes (CAN). In Table 2.1, the usual coordinate definitions used by the simulations are defined.

Detector measurements	$r_{\text{det}} = 505$	$h_{\text{det}} = 620$	
CAN measurements	$r_{\text{can}} = 705$	$h_{\text{can}} = 920$	
Coordinate definition		$z_{\text{sea}}^{(\text{bottom})} = -405.93$	$z_{\text{sea}}^{(\text{top})} = 3094.07$
CAN coordinates	$r_{\text{can}} = 705$	$z_{\text{can}}^{(\text{bottom})} = -405.93$	$z_{\text{can}}^{(\text{top})} = 508.68$

Table 2.1: *Definition of the coordinate system used for the detector in simulations as defined in the header of the simulation output files*

Figure 2.2: *Detection modules used in the KM3NeT detector. On the left side a DOM and on the right side a String, which is comprised of multiple DOMs. Taken from [Adr16].*

In Figure 2.2, the detection modules are shown. The detection volume is filled with 115 strings. On each string there are 18 **D**igital **O**ptical **M**odules (DOMs) attached. The DOMs contain 31 **P**hoto-**M**ultiplier **T**ubes (PMTs). ORCA (**O**scillation **R**esearch with **C**osmics in the **A**byss) has the same specifications as ARCA, but the DOMs are spaced differently. This array of detection modules is used to detect radiation of particles passing through or reacting near the detector volume [Adr16].
After the PMTs register the light, different triggering algorithms are run. These algorithms are still in development and can be broken down into three categories.

Trigger level	procedure	location
L0	threshold for analogue pulses (typically 0.3 photo electrons)	off shore
L1	Two L0 hits (coincidence) within a time window (typically 10ns)	on shore
L2	Making use of the orientation of PMTs	on shore

Table 2.2: *The three trigger levels planned for the ARCA detector [Adr16]*

A typical muon event trigger consists of a directional filter and sky scan to exclude atmospheric muons and other unwanted sources. For showers, the distances between hits filters PMTs, which don't have to be considered due to photon absorption. Both of these triggers belong to the L2 triggering stage.

Since PMTs are the fundamental detection module, I will briefly describe their functionality [Ham07] with the Figure 2.3.

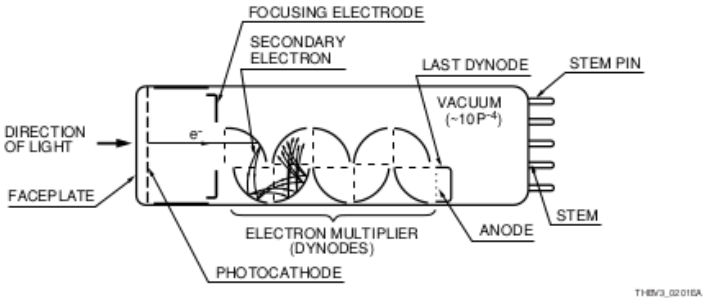

Figure 2.3: *Functionality of a photo-multiplier tube taken from [Ham07]*

Light which enters the PMT produces an output signal by the following process:

1. Light passes through the input window
2. Light excites electrons in the photocatode and the electrons are emitted into the vacuum
3. The emitted photo electrons are accelerated and focused onto the first dynode. The signal is then amplified by means of secondary electron emission. This process is repeated for multiple dynodes (usually becoming more and more positive)
4. The multiplied electrons are then emitted from the last dynode onto the anode

The signal from the anode is a voltage which depends on the specific configuration of the PMT, which is still being investigated for KM3NeT. The voltage signal is not stored. The only information kept is the initial photon hit time and the time over threshold. The time

over threshold is the time during which the output voltage is higher than a fixed threshold. It is a measure for the amount of photons, which hit the PMT during a narrow time window. In Figure 2.4 are pictures of the photo multipliers used in the ARCA detector:

(a) *ETEL D792KFL* **(b)** *Hamamatsu R12199-02*

Figure 2.4: *The two PMT models used in the detector taken from [Ham07]*

The Hamamatsu R12199-02 has a spectral response between 300 and 650 nm with a maximum at 440 nm [Ham15]. The ETEL D792KFL has no publicly available data sheet.

3 Theoretical background

A more elaborate discussion on the theoretical background of neutrino telescopes can be found in [Kat12].

3.1 Atmospheric showers

Atmospheric showers are created by interactions of vertical primal cosmic rays in the atmosphere. These charged particles with very high energies enter the atmosphere and electromagnetically interact with atmospheric particles. From the initial vertex downwards a shower of secondary particles is produced.

In the actual detection phase, atmospheric showers are mostly considered background. There are some physical studies planned concerning them, but they have low priority compared to neutrino analysis. Air showers are produced by cosmic rays. There are two types of cosmic rays, **primary** and **secondary**. Primary cosmic rays are of extraterrestrial and usual extra-solar origin. Secondaries are the products of primaries' reaction with interstellar gas and the earth's atmosphere.

The only significant intrasolar contribution to cosmic rays are solar flares. Due to the modulation by solar activity, the cosmic ray spectrum depends on time and location of observation. The main component of cosmic rays are charged particles with lifetimes above 10^6 yr, so mainly protons, some electrons and nuclei of stable atoms.

The energy range of cosmic rays is very large, but most particles have an energy around a few GeV. There are also less common cosmic rays with larger energies with the largest recorded instance being the Oh-My-God particle at 3×10^8 TeV. These cosmic rays are called **U**ltra-**H**igh **E**nergy **C**osmic **R**ays (UHECR). The interaction of charged particles with matter is usually examined in particle accelerators like the **L**arge **H**adron **C**ollider (LHC) in Geneva, but the energies of UHECR are far above the particle energies of any particle accelerator. Thus studies at high energies have to be done with cosmic rays.
The intensity in relation to the energy follows a power law with several kinks, where the spectral index α changes.

$$I_N(E) \approx 1.8 \times 10^{-4} \left(\frac{E}{\mathrm{GeV}}\right)^{-\alpha} \frac{\text{nucleons}}{\mathrm{m^2\,sr\,s\,GeV}} \tag{3.1}$$

A plot of the full flux can be seen in Figure 3.1.

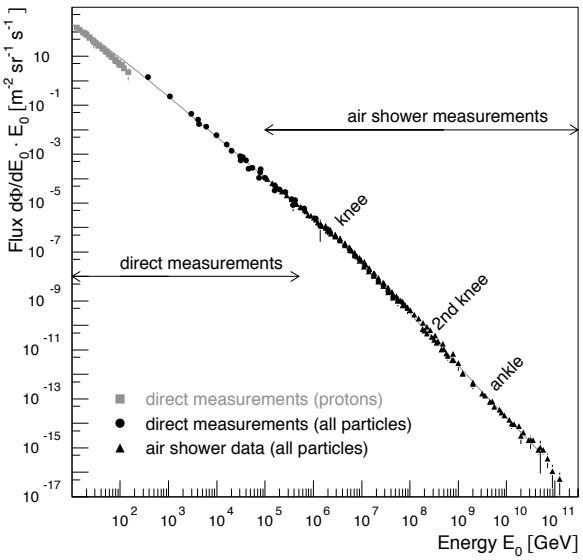

Figure 3.1: *The cosmic-ray spectrum for all particles. The spectral index below the knee is 2.7 and steepens to 3.0 until the ankle. From there on it becomes 2.7 again. The energy range up to* 10^6 *GeV is from direct measurements and the energy range above that from air shower measurements. Taken from [BEH09](Figure 1)*

The exact form of the spectrum is an indicator for the origin of the cosmic rays. The sources for rays up to and somewhat below the first knee are of galactic origin. The main candidate for these are supernova remnants. Most cosmic rays between the knee and the ankle are also of galactic origin, but no supernova remnants since they don't have enough power output. The accelerators in this region are pulsars and binary systems with one black hole as partner. Above the ankle almost all cosmic rays are assumed to be of extragalactic origin. Sources for extragalactic rays are starburst galaxies, active galaxies and gamma ray bursts [Kat12].

Muons and neutrinos are end products of the decay of heavy charged mesons, for example ones containing a **charm** or a **bottom** quark, whereas protons and electrons are products of the decay of neutral mesons. Muons and neutrinos have a much larger range than electrons and photons at high energies, so most of the atmospheric shower arriving in the detector are muons and neutrinos. Since muons interact far more than neutrinos, they are easiest to detect, making them the most relevant part of the shower.

Since the energy of the initial particle is very high and therefore the reaction is highly relativistic, the angles between muons produced in air showers are very small. This explains, why atmospheric muons arrive as bundles in the detector. Other particles from air showers are also produced in bundles, but electrons stop far before they reach the detector and the interaction probability of neutrinos is so low, that the detector will only ever pick up on one of the bundle neutrinos. [Pat16].

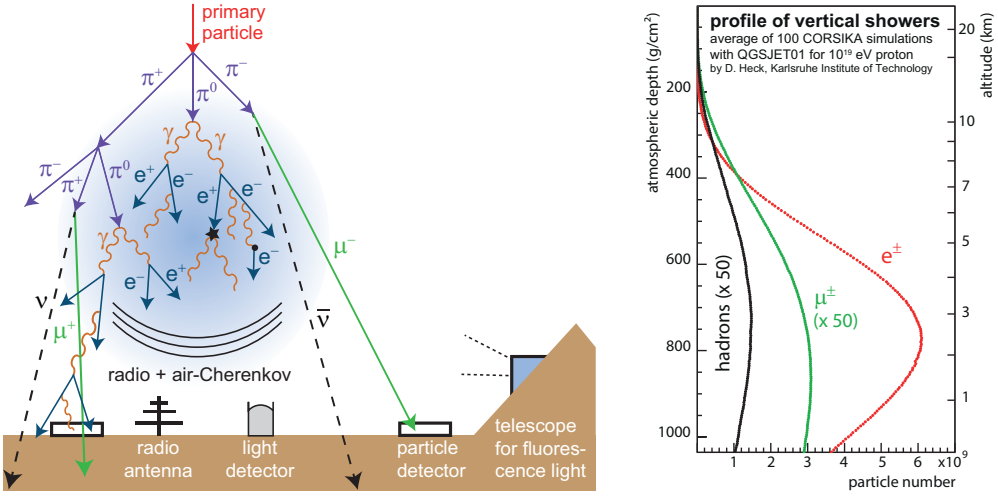

Figure 3.2: *Left: Simplified sketch of an air shower and detection possibilities. The showers contain more particles, but the ones shown are the most important in detection. Right: Longitudinal shower profile for different particle types. Taken from [Sch16](Figure 2).*

The neutrino flux generated by atmospheric showers as illustrated in Figure 3.2 can be separated into two categories, the prompt and the conventional flux. The conventional flux dominates neutrino data in underwater or under-ice detectors in the GeV - 1 TeV range. It is produced by decaying kaons and pions from atmospheric showers. Prompt flux neutrinos have much higher energies and are produced by the decay of heavy mesons usually containing a **charm** quark. Although the prompt flux neutrinos have much higher energy, their flux is strongly suppressed compared to the conventional flux [Sch13].

Spectra of extensive air shower particles

The spectrum of prompt and conventional neutrino fluxes has been calculated in [Enb08] and is illustrated in Figure 3.3.
For the Gaisser and Honda calculation [GH02], the conventional flux seems to follow the flux of the cosmic-ray spectrum quite closely. A little below 10^6 GeV, there is a kink in the flux just like in the cosmic ray spectrum. The conventional flux behaves differently

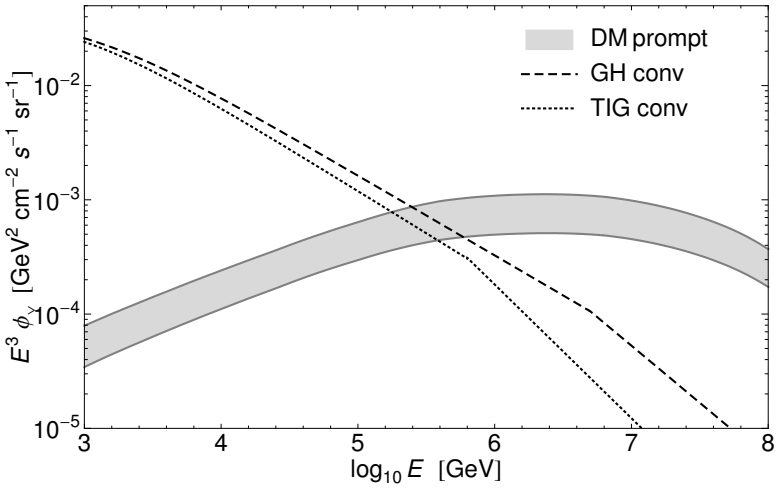

Figure 3.3: *The prompt and conventional flux of muon neutrinos created from primal cosmic ray interactions with two different calculations of the conventional flux. Taken from [Enb08](Figure 5).*

from the cosmic ray flux. Although the cosmic ray flux still follows a power law, the prompt flux flattens. It does not share any similarity with the cosmic ray flux.

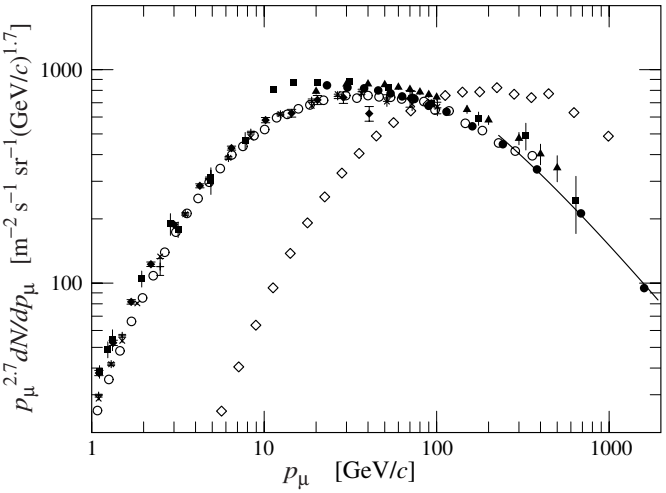

Figure 3.4: *Differential spectrum of muons times E^2 from vertical air showers at at sea height. All but $\diamondsuit are for \theta = 0°$ and $\diamondsuit is for \theta = 75°$. Taken from [Pat16].*

In Figure 3.4, a calculation of the muon flux at sea level from cosmic ray interaction is shown. Almost all of the muon differential spectrum is below 1 TeV. This is reflected in the MUPAGE event files (see subsection 4.1.1), which rarely have any muons with energies above 1 TeV. The only reason why these muons provide a significant background

is that they come in bundles of 1-100 muons.

Since the muons come in bundles, their energy loss behavior should be roughly like that of one low energy muon times the number of muons in the bundle. Of course this is only an approximation, since the bundle does have some lateral distribution. Since the main contributions to stochastic energy losses become more significant at higher energies, the energy loss spectrum should be much smoother than that of single high energy muons.

Cosmic ray particles stemming from extensive air showers are considered background, since they provide no information about their origin in the universe. Cosmic rays are charged particles, which are deflected on their path to earth by coulomb interaction. This is not the case for very high energy neutrinos, which barely interact with matter on the way to earth. Since extensive air showers are only caused by charged particles, they have a high chance of no longer having their initial direction. Thus they do not yield information on their origin. Using energy cuts on neutrinos and track property cuts on muons, it should be possible to filter most of the atmospheric shower background, but the prompt neutrino flux still constitutes a diffuse neutrino background that physically limits the precision of the experiment. A reason for the importance of muon bundles is, that atmospheric neutrinos are usually accompanied by them. Thus an identification of a muon bundle can veto a atmospheric neutrino.

3.2 High energy neutrinos

As already discussed in the previous section, high energy neutrinos from extraterrestial sources constitute a great telescope for distant astronomical objects due to the neutrinos' low interaction rate.
These high energy neutrinos are produced by primal cosmic ray interactions, but in contrast to atmospheric muons, these interactions happen extraterrestially with matter or radiation fields ambient to the initial accelerator mainly due to processes described in Equation 3.2 and Equation 3.3.

$$p + \text{nucleus} \rightarrow \pi + X \quad (\pi = \pi^{\pm}, \pi^0) \tag{3.2}$$

$$p + \gamma \rightarrow \Delta^+ \rightarrow \begin{cases} \pi^0 + p \\ \pi^+ + n \end{cases}, \tag{3.3}$$

and subsequently

$$\pi^0 \rightarrow \gamma\gamma\,, \qquad \pi^{\pm} \rightarrow \mu^{\pm}\overset{(-)}{\nu}_{\mu}\,, \qquad \mu^+ \rightarrow e^+\bar{\nu}_{\mu}\nu_e\,, \qquad \mu^- \rightarrow e^-\nu_{\mu}\bar{\nu}_e \tag{3.4}$$

taken from [Kat12].
The interaction of these primal cosmic rays becomes more and more diffuse the further

away from the initial accelerator they are. So from the perspective of the earth, these accelerators seem like neutrino point sources. The total spectrum of neutrinos arriving in the detector amounts to the flux plotted in Figure 3.5.

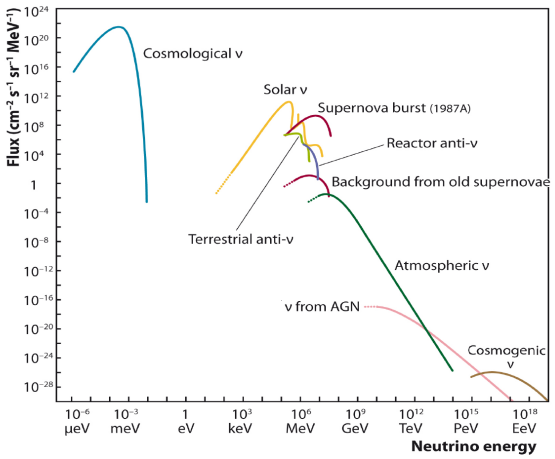

Figure 3.5: *Flux of all neutrinos (including atmospheric contributions) in dependence of energy. Taken from [Kat12](Figure 1).*

Since the sensitivity of the detector is in the TeV regime, mainly atmospheric and AGN contributions are relevant.

The low interaction rate makes the detection of neutrinos very difficult. Since neutrinos are not charged, there is no way to observe them directly with a light based measurement apparatus. So what is measured, are charged reaction products from neutrino interactions. These interactions are rare, but can easily be resolved with a large detector volume and instrumentation density. Since the neutrinos travel a long path from their source, neutrino oscillations transform the initial flavor distribution into 1:1:1 ($\nu_e : \nu_\mu : \nu_\tau$). Contrary to solar or reactor neutrinos, the ratio of anti-neutrinos and neutrinos is almost one. At high neutrino energies deep inelastic scattering with nuclei dominates the interactions. It is important to differentiate charged and neutral current interactions.

Charged current interaction

$$\overleftrightarrow{\nu}_\ell N \to \ell^\mp X \tag{3.5}$$

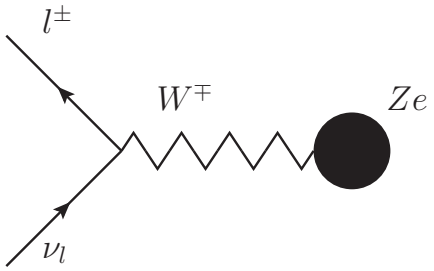

Figure 3.6: *Feynman diagram of a charged current interaction. The incoming neutrino ν_l interacts via a $W^{\pm}$ boson with the nucleons to an outgoing charged lepton $l^{\mp}$.*

This interaction is called charged current interaction (see Figure 3.6 and Equation 3.5) since the boson exchanged is $W^{\pm}$. The y axis is time and the x axis is spatial in Feynman diagrams from now on. If a neutrino does have a charged interaction near the detector volume, there is a $\frac{1}{3}$ chance for it to be a $e^{\pm}$, $\mu^{\pm}$ or $\tau^{\pm}$. The three particles have very distinct energy loss patterns. The most favorable reaction outcome is a muon since the reconstruction of muons has the largest directional resolution. This is due to the fact, that tauon and electron interactions are both shower like and muon interactions are track like. Since $\mu^{\pm}$ have a longer mean free path than $e^{\pm}$ and $\tau^{\pm}$, the effective detection volume is also much larger.

An event is called a shower like event, if the photons propagate in a sphere from one point. A track like event on the other hand is a concatenation of electromagnetic cascades along a straight line (see Figure 3.7).

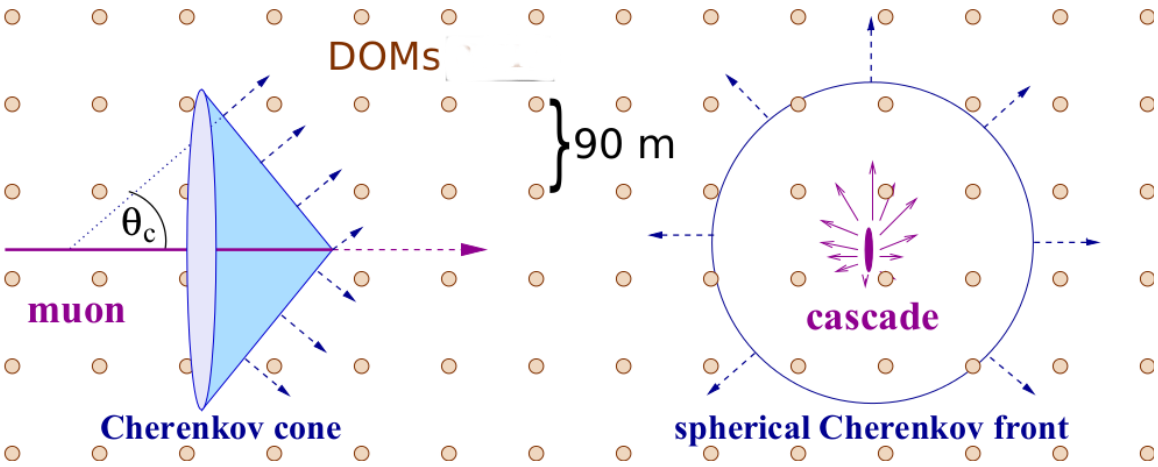

Figure 3.7: *On the left a typical track like muon event is shown. On the right side, a shower like energy loss is shown. Every brown dot indicates a DOM. Taken from [Kat12](Figure 11).*

Neutral current interaction

$$\overset{(-)}{\nu}_{\ell} N \rightarrow \overset{(-)}{\nu}_{\ell} X \tag{3.6}$$

The Figure 3.8 corresponds to Equation 3.6.

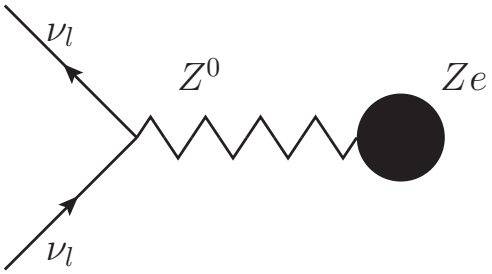

Figure 3.8: *Feynman diagram of neutral current interaction. The incoming neutrino interacts via a Z^0 boson with the nucleons to an outgoing neutrino of the same type.*

Neutral current interactions (see Figure 3.8 and Equation 3.6) look very different from charged current interactions since the products of a neutral current interaction are a neutrino and hadrons. A charged current interaction has at least two points of photon emission, the initial interaction and some interaction of the resulting charged particle. There is only a single hadronic shower at the initial interaction vertex due to the neutral current interaction.

3.3 Cherenkov light

The fundamental physical phenomenon used to detect particles in neutrino telescopes is electromagnetic radiation. For particles in dielectrica moving at velocities larger than the speed of light in that medium, the angle of light emission is at a specific angle (see Figure 3.9). This angle is called Cherenkov angle. It is best made plausible with a graphic.

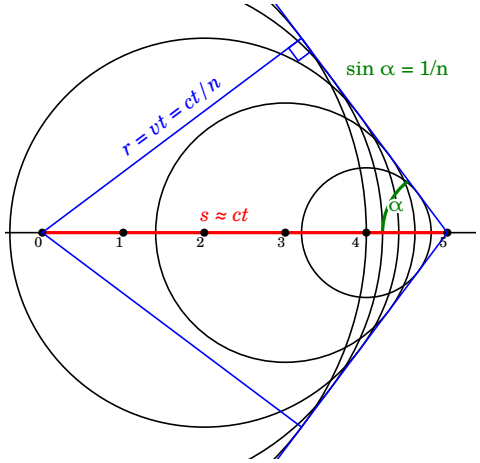

Figure 3.9: *A sketch on how relativistic signal transmission leads to the Cherenkov angle. This figure assumes, that the particle is moving close to the speed of light in vacuum. (from wikimedia commons)*

Assume there is a charged particle, that moves with a velocity $v > \frac{c}{n}$ along a straight line. Take some point, where the particle emits a photon due to electromagnetic interaction and define it as the coordinate center. Now propagate the photon and particle in time and assume they form a wavefront. This means, that the angle between photon velocity and the distance vector between the two photons has to be 90 degrees. Otherwise the two photons would be moving into different directions. For the photons to be coherent, the times at which both photons reach the wavefront have to be equal. The muon travel time is

$$t_\mu = \frac{d_\mu}{v_\mu} = \frac{d_\mu}{\beta_\mu c} \tag{3.7}$$

and the photon travel time is

$$t_p = \frac{n \cdot d_p}{c} = \frac{n \cdot d_\mu}{c} \cos\theta\,. \tag{3.8}$$

Requiring these times to be equal yields

$$\cos\theta_{ch} = v\frac{c_m}{c_0} = \frac{v_\mu}{n} \tag{3.9}$$

which reduces to

$$\cos\theta_{ch} = \frac{c_m}{c_0} = \frac{1}{n} \tag{3.10}$$

for muons with energies considered in the experiment. In general n depends on the wavelength of the emitted light. For water the refractive index ranges from 1.33 to 1.35 in the visible spectrum.

The energy emitted by this process is modeled by the Frank-Tamm formula

$$\frac{\mathrm{d}N}{\mathrm{d}x\mathrm{d}\lambda} = \frac{2\pi\alpha}{\lambda^2} \cdot \left(1 - \frac{1}{\beta_\mu^2 \cdot n(\lambda)^2}\right) \tag{3.11}$$

for the spectral Cherenkov photon emission distribution for particles with ± unit charge. So the total energy loss one can obtain by integrating this expression is

$$-\frac{\mathrm{d}E}{\mathrm{d}x} = \frac{2\pi\alpha h}{c} \int \nu \left(1 - \frac{1}{\beta_\mu^2 \cdot n^2(\nu)}\right) \mathrm{d}\nu \tag{3.12}$$

for $\beta_\mu \cdot n \geq 1$.
For a given medium $\lim_{\beta\to 1} -\frac{\mathrm{d}E}{\mathrm{d}x} = \frac{2\pi\alpha h}{c} \int \nu \left(1 - \frac{1}{n^2(\nu)}\right) \mathrm{d}\nu$ = const. The larger β, the more energy is lost on a given path element. So it follows, that lighter particles lose more energy than heavier ones since they tend to be faster. This implies, that electrons travel a shorter path length than muons before stopping.

3.4 Energy losses for muon tracks

An important fact about the emitted radiation is scattering and absorption of light in water. Figure 3.10 shows these quantities in relation to the wavelength of the corresponding light.
The scattering length shows a linear dependence on the wavelength with a slope of about $0.2\,\frac{\mathrm{m}}{\mathrm{nm}}$. The absorption length shows a Gaussian behavior with a peak of 63 nm at 444 meters. The center position of the Gaussian is compatible the specifications of the PMTs used (see chapter 2).

As is known from the energy loss diagram in Figure 3.11 for muons in copper, at energies above 1 TeV mainly radiative energy losses are relevant for the behavior of a charged particle. The energy loss mechanisms, which are important at lower energies are mostly of electronic nature. They can be divided into energy losses due to excitations of matter and ionization (minimum ionizing track). I will only discuss the radiative energy losses in detail.

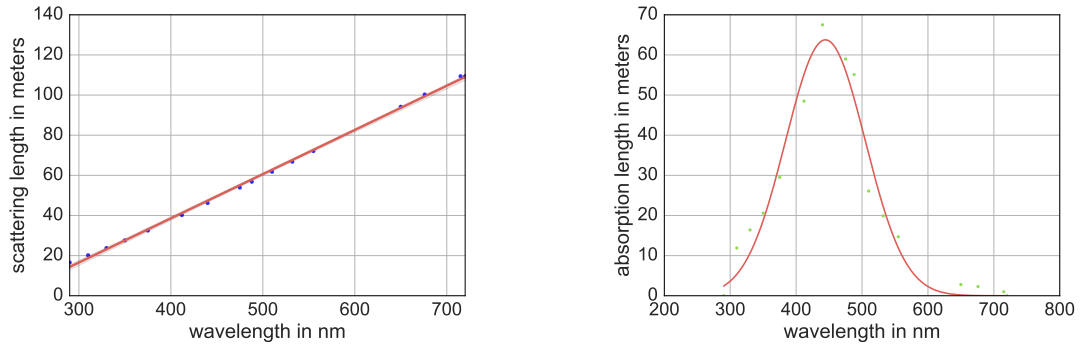

Figure 3.10: *Scattering (left) and absorption (right) length in seawater in dependence of wavelength used in the KM3NeT codes*

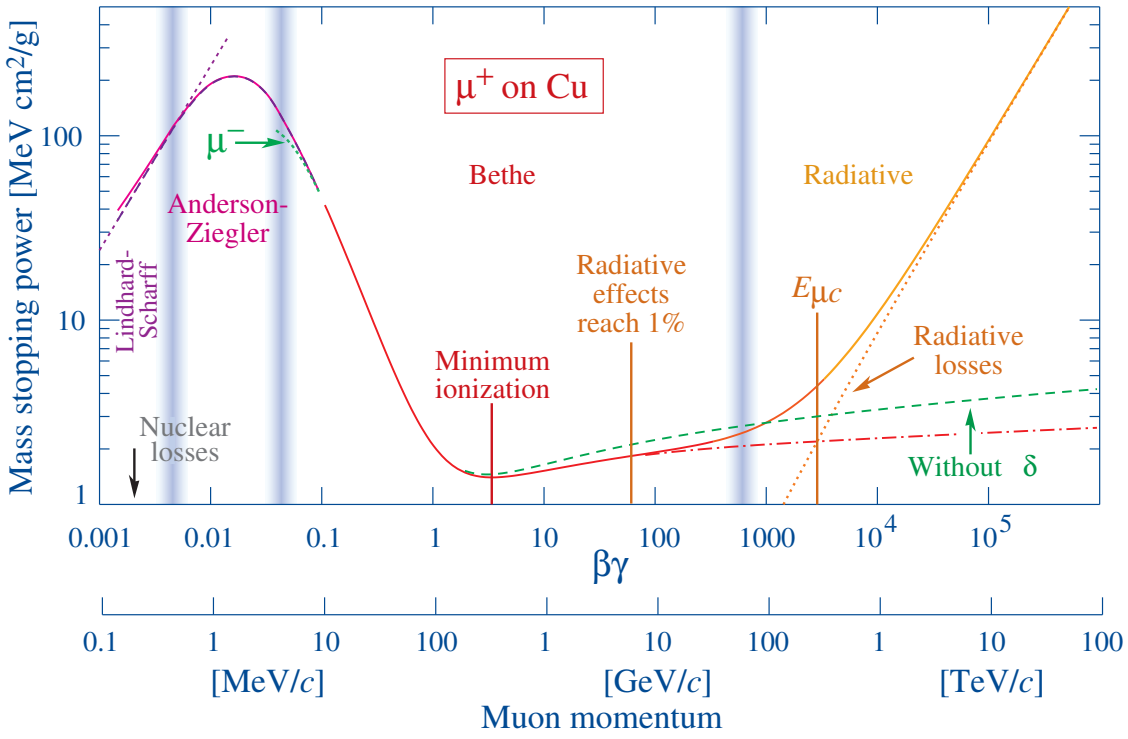

Figure 3.11: *A plot of energy loss for muons in copper against the total muon energy. Different sections are related to different physical processes and described by different models. Taken from [Pat16](Figure 32.1)*

The significant contributions to radiative energy losses are photonuclear interaction, bremsstrahlung and pair production. Another relevant contribution to muon energy losses are ionizing effects. In general, the radiative energy losses are classifiable as sudden and

stochastic, whereas the ionizing energy losses have a smooth and continuous character. A simple model for muon energy lost is

$$L(E) = \alpha(E) + \beta(E)E \tag{3.13}$$

where α describes ionizing energy losses and

$$\beta(E) = \beta(E)_{\text{brems}} + \beta(E)_{\text{e}_+/\text{e}_-} + \beta(E)_{\text{photonuclear}} \tag{3.14}$$

describes radiative energy losses. $\beta(E)$ is a slowly varying function of the energy. A more detailed discussion on the calculation of these contributions can be found in [KBS01], who have calculated a visual representation of the energy dependence of energy losses for high energy muons in pure water which is plotted in Figure 3.12.

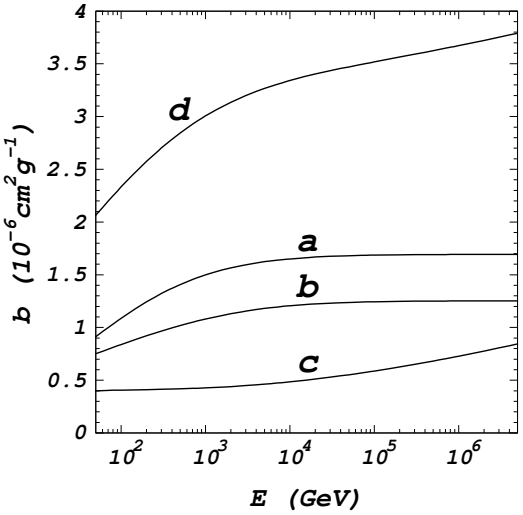

(a) *Plot of the radiative losses in terms of E, where* `a` *is pair production,* `b` *is Bremsstrahlung and* `c` *is photonuclear interaction.* `d` *is the sum. Taken from [KBS01](Figure 1)*

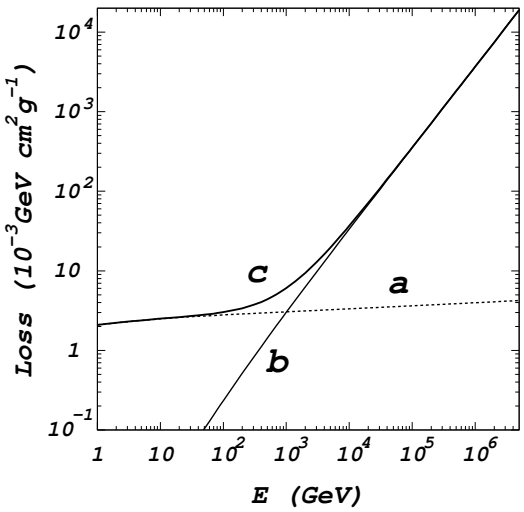

(b) *Plot of the total energy loss function L(E).* `a` *is a plot of the ionization term and* `b` *the radiative term.* `c` *is the sum. Taken from [KBS01](Figure 2)*

Figure 3.12: *Plots of muon energy loss contributions.*

The ionizing energy losses are still relevant around 1 TeV, but quickly become insignificant in the 10 TeV range and above. The different contributions to the radiative energy losses change slightly over the energy range. Since large energy losses are stochastic, the background due to ionization is important even for muons with energies of several TeV.

3.4.1 Photonuclear effect

Hadronic cascades for neutrino events can be induced by either neutral current interactions or by photonuclear interaction. These two energy loss types are fundamentally different

in the sense that during an NC (neutral current) interaction, the neutrino looses energy, whereas the muon looses energy in a photonuclear interaction.
The photonuclear effect is inelastic lepton-nucleon or lepton-nucleus scattering, described by

$$l + N \rightarrow l + \text{hadrons} \tag{3.15}$$

making it a hadronic effect by definition. Since a lepton and another charged particle are interacting, this process is electromagnetic (see Figure 3.13). Figure 3.12a shows, that the contribution from the photonuclear effect to the radiative energy losses is about $\frac{1}{4}$ of the total in the energy range of interest (1 TeV - 1 PeV). $\frac{1}{3}$ of neutrino interactions and $\frac{1}{4}$ of all muon energy losses are hadronic. Hadronic cascades are less collimated than electromagnetic cascades due to the higher weights of the produced particles making it harder to reconstruct directional information.

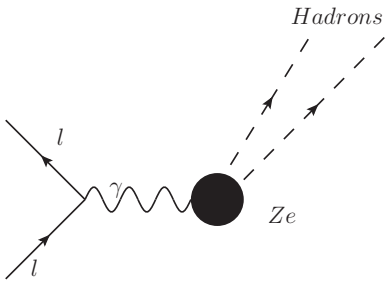

Figure 3.13: *Feynman diagram of photonuclear interaction. The incoming lepton l interacts electromagnetically with the nucleons of a neighboring nucleus with charge Ze to produce a lepton l and hadrons.*

The resulting hadrons from the interaction in Figure 3.13 then form a hadronic cascade similar to extensive air showers but with far less energy.

3.4.2 Bremsstrahlung

Bremsstrahlung, in general, is caused by the deceleration a particle experiences, when it is deflected by charged particles. For electrons, bremsstrahlung is the main energy loss mechanism. For muons however, the energy loss is suppressed by $\left(\frac{m_e}{m_\mu}\right)^2 = 2.33901 \times 10^{-5}$, so direct pair production and hadron production are also important. Direct pair production is the largest contribution of these three. The process of bremsstrahlung is depicted in Figure 3.14.

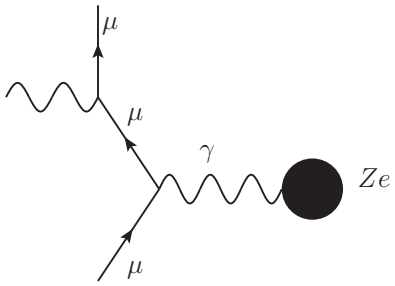

Figure 3.14: *Feynman diagram of bremsstrahlung. The incoming muon μ interacts electromagnetically with some ambient nucleus and emits a photon shortly afterwards*

This type of energy loss is highly stochastic in all of the considered energy ranges. It can be shown, that the total power radiated P is described by the covariant formula

$$P = -\frac{2}{3}\frac{q^2}{m^2 c_0^3}\frac{dp_\mu}{d\tau}\frac{dp^\mu}{d\tau} \tag{3.16}$$

This explains the aforementioned suppression of the energy loss by the mass fraction squared. Electrons show shower-like behavior since their radiated power is so large due to their small mass. Tauons on the other hand look like two consecutive shower events since the initial interaction produces a shower and the decay produces one.

3.4.3 Direct pair production

Direct pair production is the process in which a high energy muon produces an electron-positron pair as it passes through the electric field of a nucleus. It is best described with the Feynman diagram in Figure 3.15.

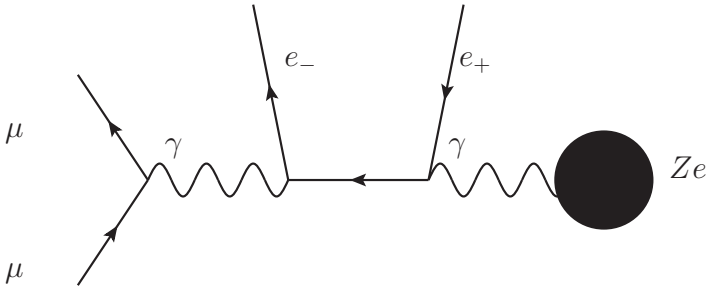

Figure 3.15: *One of the Feynman diagrams of direct pair production. Here an incoming muon μ emits a photon γ_1 which undergoes pair production to $e^\pm$. This pair then Coulomb interacts with a close nucleus in order to conserve energy and momentum*

So the reaction is described by

$$\mu + \text{nucleus} \rightarrow e^+ + e^- + \text{nucleus} + \mu\,. \tag{3.17}$$

Energy losses due to pair production are also highly stochastic, especially at high muon energies. At smaller muon energies, the direct pair production contribution is almost smooth.

3.4.4 Electromagnetic cascades

Electromagnetic cascades are caused by direct pair production processes or high energy bremsstrahlung, that result in charged particles causing more pair production and bremsstrahlung (see Figure 3.16).

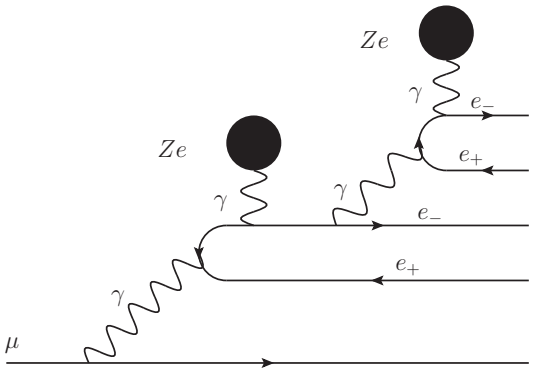

Figure 3.16: *Sketch of an electromagnetic cascade. Photons decay due to pair production and electrons due to bremsstrahlung. For illustrative purposes, time and spaces axes have been switched.*

An electromagnetic cascade is caused by the emission of a single high energy photon. This photon produces an electron-positron pair which has to interact with a nucleus in order to conserve energy and momentum. Without matter, only virtual electron-positron pair production is possible. The resulting high energy electrons, positrons and photons produce their own electromagnetic shower contributing to the cascade. These showers are best characterized by the radiation length X_o which is defined such that

$$-\frac{\mathrm{d}E}{\mathrm{d}x} = \frac{E}{X_0} \tag{3.18}$$

for the energy loss of an electron by bremsstrahlung. The radiation length is a material constant and is 36.08 $\frac{\mathrm{g}}{\mathrm{cm}^2}$ for pure water.

The reason for the usefulness of this parameter is, that the mean free path of pair production for a photon λ_γ and the mean free bremsstrahlung path for an electron λ_{e^-} can be related to it by Equation 3.19.

$$\lambda_\gamma = \frac{7}{9} X_0 \,, \qquad \lambda_{e^-} = X_0 \,. \tag{3.19}$$

Since these two effects constitute an electromagnetic cascade, the radiation length describes the range of one. The stochastic nature of bremsstrahlung and pair production implies that electromagnetic losses seem like randomly distributed energy loss peaks on the muon track.

4 Simulation and reconstruction

The work done with simulated data can be broken down to two parts. The first part is the actual simulation. In the case of the KM3NeT collaboration, a Monte Carlo chain is used. The second part is the analysis of the simulated data. These are programs which reconstruct particle trajectories and information about the particle's energy.

4.1 Monte Carlo chain

The simulation also is divisible into three major parts. The particle generation and if necessary initial interaction, the muon propagation, light propagation and the detector response. The background simulation is usually part of the last step. The only difference between muon bundles and neutrinos is the initial particle generation. The rest can be done with the same programs since both event types are muonic.

4.1.1 Particle generation

Particle generation algorithms have varying degrees of freedom. If the algorithm simulates most of the physics involved, many values like the branching ratio of a certain reaction, can be set. If the algorithm is fast and therefore only based on a parametric model, one may only use simple variations of that model. From the values of the model parameters, so called weights can be calculated. The simulation files used in this thesis have 3 weights:

Label	Name	Related to
w1	-	generation volume or surface
w2	generation weight	weight for neutrino flux
w3	global weight	particle rate

Table 4.1: *Details on weights used for particle generation*

So the weights describe the detector response (w1), the differential flux (w2) of particles and the total flux of particles (w3). The weights are not entirely independent. Especially weights 2 and 3 are related.

Muon bundles:

The program used to generate muon bundles is called MUPAGE (Atmospheric **MU**ons from **PA**rametric formulas: a fast **GE**nerator for neutrino telescopes), which was designed for neutrino telescopes underwater. MUPAGE simulates events at the surface of the CAN volume. Since atmospheric muons can only move downwards, the direction and angle of these events are also restricted. The parameters for the flux of muon bundles, such as the energy spectrum and the spread in dependence of depth and zenith angle are defined by parametric formulas. These formulas are given by a primary cosmic flux model constrained by experiment [Car09]. Since MUPAGE is based on a simple parametric physical model, most parameters are fixed and only fluxes proportional to the given one can be simulated. In conclusion, the weights can not be modified freely. This is sensible since there are far more muon bundle events than neutrino events for the detector and they are mainly considered unwanted background. The muon bundle generation used in this thesis only produces muon bundle with energies above 10 TeV.

Neutrinos:

The program used to generate neutrino events is called genhen v7r6 (**GEN**erator of **H**igh **E**nergy **N**eutrinos). It uses a more detailed physical simulation. Using a user specified neutrino spectrum and models for neutrino interaction cross section, atmospheric neutrino fluxes and the absorption of the earth, genhen calculates the weights used in event generation. This gives the user freedom to essentially choose weights freely. As a side effect, one can choose to use physically motivated weights if it is important to do so or one can choose not to. In my case, unphysical weights were chosen, since I try to characterize features specific to single high energy muons, regardless of the underlying generation model [Dav02].
The particle generation also includes the initial neutrino interaction. The code used for this is called LEPTO, a Monte Carlo program to simulate complete events in deep inelastic lepton-nucleon scattering [Ing97]. The resulting particles including the muon are used to propagate the event further.

4.1.2 Particle propagation

The program used for particle propagation is called km3. It includes muon propagation and photon propagation for high energy muons in the detection volume. The muons are propagated using a code package called MUSIC (**MU**on **SI**mulation **C**ode). MUSIC is a three dimensional muon propagation code using a detailed physical model which applies recent calculations of cross sections to calculate energy losses and angular deviation of the muon track [Car09]. The code was modified to operate by binning the muon path into 4 m segments in order to increase performance. For each segment an energy loss is calculated and a random position within this 4 m segment is assigned.

Due to the large amount of photons emitted and the many interactions those partake in, it is impossible to simulate all emitted photons. So km3 operates using precomputed photon tables. The tables store the distribution of numbers and arrival times of PMT hits at different distances, positions and orientations with respect to the point of emission. This data is used for calculating the detector response. There are three types of photon tables. A table for the minimal ionizing muon track, a table for the ionizing electrons accompanying it and several tables for higher stochastic energy losses. The tables for stochastic energy losses are electron tables of the corresponding energy. In this fashion it is possible to simulate smooth and point like energy losses.

4.1.3 Detector response

Both detector response and background simulation are performed by JTriggerEfficiency. Simulating the detector response means simulating how the detection modules will react to the light generated from km3. A PMT hit at time t and position x and the initial conditions of the PMT are propagated to yield the PMT signal. The PMT signal consists of the initial hit time t_{initial} and the time over threshold t_{tot} during which the PMT signal voltage is over some threshold. JTriggerEfficiency also simulates triggering algorithms which correspond to the discussed trigger levels to some degree. At this point, the simulated trigger algorithms are not necessarily equivalent to the ones discussed earlier and in the letter of intent since they are still up to discussion.
JTriggerEfficiency also handles the background calculation due to K40[1] background. Other background sources exist, for example bioluminescence, but are not simulated.

4.2 Reconstruction

Depending on the type of event and the specific reconstruction chain used, the reconstruction has different steps.
Parameters reconstructed usually contain position and direction and several quality parameters signaling the code's confidence in its reconstruction. Some reconstructions also perform an energy fit.

4.2.1 Shower reconstruction: aashowerfit

Aashowerfit is the standard shower reconstruction used in the current reconstruction chain. It implements different shower fitting algorithms. These algorithms can be divided into two categories:

1. Time residual based

[1] K40: Potassium 40

2. Poisson PDF[2] based on P(hit—no hit)

Before any reconstruction, aashowerfit performs hit merging and hit selection. Hit merging can be defined as follows: Take a given PMT with more than one hit. Now take the time of the first hit. Then define a lattice starting at this point with spacing t_{cluster} and for every bin in this lattice only keep the first hit. Now the hits on this PMT have all been merged into the first hit.

The hit selection is performed by defining so called coincidences and only keeping coincident hits and omitting all others. A coincidence hit is defined as two hits after hit merging on a DOM, which happen within a given time window t_{coinc}.

Time residual based

The largest multiplicity coincidence of first coincidences on all DOMs is used as starting point, the so called pivot hit. The number of hits associated with a pivot hit is strongly energy dependent. A position is fitted using this pivot position by means of a minimum estimator operating on the score function. To define the score function, time residuals have to be defined:

$$t_{\text{res}}(h,p) = h_t - p_t - \frac{\|p_{\text{pos}} - h_{\text{pos}}\|}{v_{\text{light}}}\,. \tag{4.1}$$

First all time residuals which are larger than 800 ns or smaller than -800 ns are filtered to reduce background due to scattering and computation time. Using these hits, the score function can be defined. The score function m is a likelihood for a cascade with the given parameters.

$$m(p_{\text{shower}}) = \sum_{h\in\mathcal{C}} h_{\text{counts}} \cdot \sqrt{1 + t_{\text{res}}(h, p_{\text{shower}})^2} \tag{4.2}$$

Where h_{counts} is the number of hits for the coincidence after merging and p_{shower} are the shower hypothesis position and time, which are minimized. This is the implementation of a reconstruction using time residuals and it is used as a fit for the position and time of a shower.

Poisson based

The Poisson based analysis is used to reconstruct energy and direction. First, all hits with time residuals smaller than -100 ns and larger than 900 ns are filtered out. Starting from the shower position that has been reconstructed, the algorithm determines the distance vector between DOM and shower position $\vec{v}_d$. There are different computation methods, which use different technical implementations of the same method for speedups.

[2] PDF: Probability density function

I will explain one of the methods since the details are only technical. The algorithm evaluates a histogram to get the mean number of photons detected from a 1 PeV shower, $\mu(1\,\mathrm{PeV})$. This 3D histogram depends on $\alpha(\vec{H}, \vec{v}_d)$, $\alpha(\vec{H}, \vec{P})$ and $\|\vec{v}_d\|$ with the hypothesis direction $\vec{H}$ and the PMT direction $\vec{P}$. μ can easily be calculated for other energies via $\mu(E) = \frac{E}{E_0}\mu(E_0)$ (see the theory for muon energy losses). Since the problem is counting how many photons hit a given PMT, a Poisson probability distribution is a reasonable choice since there are a lot of hits per event. Thus the probability of a PMT not being hit at a given energy is approximately

$$P_0 = \exp(-\mu(E) - \mathcal{N}(\mathrm{K40})) \tag{4.3}$$

where $\mathcal{N}(\mathrm{K40})$ is the average number of hits on a PMT due to K40 background.
With this probability, a reasonable likelihood for the hit PMTs can be constructed:

$$\log\Big(L(E, \vec{H})\Big) = \sum_{\mathrm{P}\in\mathcal{H}} \log(P_0) + \sum_{\mathrm{P}\in\mathcal{U}} \log(1 - P_0)\,. \tag{4.4}$$

The quantity $\mathcal{P}(\mathrm{k40})$ is the probability for K40 background to produce a hit. $\mathcal{H}$ is the set of all hit PMTs for an event. $\mathcal{U}$ is the set of all unhit PMTs for an event.
The resulting likelihood in dependence of the free parameters E and $\vec{H}$ is maximized. The maximization results are used as direction and energy. The energy is then corrected by means of a 2^{nd} degree polynomial fit to the median of the $\mathrm{E}/E_{\mathrm{MC}}$ distribution [A. 14].

4.2.2 Track reconstruction: JGandalf

The JGandalf reconstruction routine has multiple steps:

1. JPrefit: Scans the solid angle with an angular grid. It clusters all L1 hits in each direction. Then it performs a linear fit of (x ,y ,t) while removing outliers.
2. JSimplex: Selection of start values from JPrefit. Cluster L1 and L0 hits. Do a five parameter fit of (x, y, t, dx, dy) by means of Powell's method.
3. JGandalf: Select the N best start values from JSimplex. Use all first hits within restricted position and time space. Use the Levenberg-Marquardt algorithm to do a five parameter fit of (x, y, t, dx, dy).
4. JEnergy: Performs an energy fit using the track reconstructed by JGandalf.
5. JEvt: Transform the Jpp online format to the aanet offline format.

Additional quantities calculated, that are not apparent are $\beta_0 = \sqrt{T_x^2 + T_y^2}$ and $\beta_1 = \sqrt{T_x \cdot T_y}$ where T_x and T_y are the estimated uncertainties in the x and y direction cosines. Another quantity is L_{red} which is the likelihood divided by the number of hits related to the track.

4.2.3 Tau double bang reconstruction: Belle Starr

Belle Starr is a reconstruction written by Robert Bormuth to reconstruct tau double bang events. It is divided into three steps, the prefit, the scan and the peak identification.

Prefit

Since Belle Starr was originally programmed to reconstruct tau double bang events, which consist of two showers, the algorithm used is a small modification to aashowerfit with the parameters $t_{\text{merge}} = 20\,\text{ns}$ and $t_{\text{cluster}} = 500\,\text{ns}$. The differences are:

1. h_{counts} counts the hits per coincidence before merging.
2. Uses Monte Carlo hit times.
3. Does not filter time residuals for the position fit.

There are some technical differences in the information stored for the likelihood computation in the scan as well.

Scan

The scan defines a number of points spaced a user defined distance apart. It starts at the reconstructed position vertex and scans in the reconstructed direction and backwards. It computes the likelihood for an energy loss along this axis for every scan point. The computation of the likelihood is done similarly to the first minimization in the prefit stage. Using the same t_{res} as earlier the score is defined as follows:

$$m(p) = \sum_{\text{h}\in\text{hits}} -\log(\mathcal{PDF}(t_{\text{res}}(h, p_{\text{shower}})) + \mathcal{PDF}(t_{\text{res}}(h, p)) + \mathcal{P}(\text{k40})) \tag{4.5}$$

where $\mathcal{PDF}$ is a probability density function that gives the likelihood of an event for a given time residual. p is the scan point along the scan direction. The function is a PDF (**P**robability **D**ensity **F**unction) is precomputed and plotted in Figure 4.1.

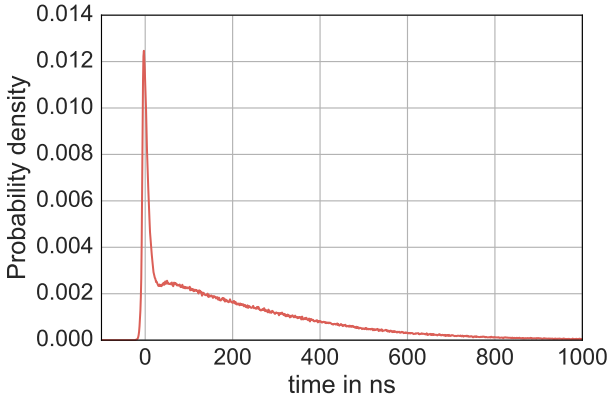

Figure 4.1: *Plot of the PDF used for the Belle Starr scan to calculate the contribution of hits with different time residuals to the likelihood*

The scan then defines the first bang of the tau double bang event as the shower reconstruction vertex minus 10 ns in time direction. This has to be done since the two close showers skew the position fit of the shower reconstruction. The second tau bang is defined by the minimum bin of the likelihood. The two bangs are then ordered such that the second bang has a higher likelihood than the first one with the physical motivation, that the second bang has more energy than the first in a tau double bang event.

Peak identification

The peak identification computes the peaks of the Likelihood given by the Belle Starr scan output using TSpectrum implemented in ROOT. This includes a simple background estimation without physical motivation.

The run time of Belle Starr on 543 muon outside of CAN events was 8785 seconds (2 hours 26 minutes 25 seconds) resulting in an average of 16 s per event. This excludes any conversion between formats, since Belle Starr can be programmed to work with any format.

5 Technical modifications performed on Belle Starr

This section discusses technical problems in the application of the tau double bang reconstruction algorithm Belle Starr and my solutions to apply it to muon event files.

5.1 JGandalf instead of aashowerfit

My first step when using Belle Starr was to substitute the standard Belle Starr prefit with input from JGandalf. The physical reason for this is apparent since tau events have two very close shower-like energy losses. So using a shower reconstruction for position and direction is sensible. This, however is not the case for muon tracks. Muon tracks consist of stochastic and continuous energy losses. The shower fit is neither optimized for the variable number of large energy losses nor does it make use of the continuous energy losses. So it would make sense for a track reconstruction to work better on muon tracks. The quality parameters are:

1. The angle Θ between reconstructed track and MC track
2. The distance d_{mest} of the initial reconstructed vertex from the MC track (the length of the orthogonal projection vector of the vertex onto the track)

These vertices have different meanings depending on the reconstruction as described in the previous chapter. It has to be mentioned that, since the JGandalf reconstruction places the vertex into the middle of the track, its results will generally be better for bad events than aashowerfit. So comparing outliers for this parameter would not be fair. I will not discuss other possible comparisons with the MC data to keep this section short since a worse position and direction reconstruction automatically result in a worse result in all following analyses. A total of 22614 single high energy muon events were used. To determine which reconstruction is better suited, define a well reconstructed event as one, that has the following properties

1. $\Theta < 1^\circ$
2. $d_{\text{mest}} < 4\,m$

and a badly reconstructed event as one, that does not. This definition of a good event has a harsh angular cut since the angular resolution is far more important when creating a scan. To decide which reconstruction is more appropriate, only areas around well reconstructed events should be considered, such that outliers do not skew the analysis.

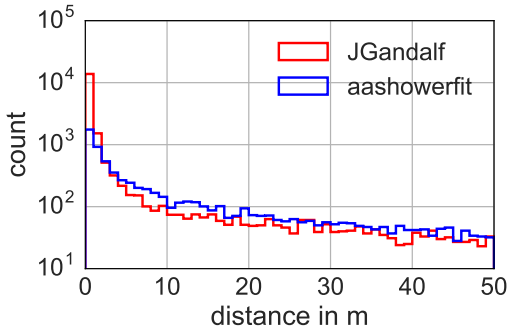

(a) *Histogram of d_{mest} between JGandalf and aashowerfit reconstruction and MC track in range* $[0\,m, 50\,m]$

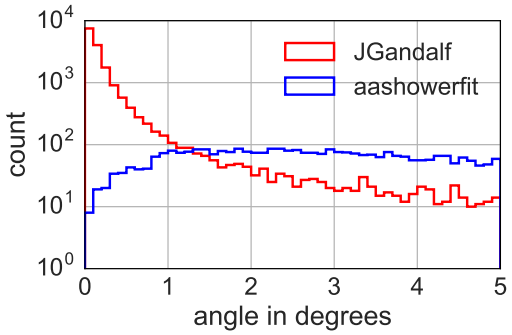

(b) *Histogram of angle between JGandalf and aashowerfit reconstruction and MC track in range* $[0°, 5°]$

Figure 5.1: *Zoomed in quality analysis to decide between aashowerfit and JGandalf*

In Figure 5.1 a clear difference in quality between the track and shower reconstruction can be observed. There is already a significantly larger number of events with a good position reconstruction in Figure 5.1a for JGandalf compared to aashowerfit, but the main difference is the angular resolution plotted in Figure 5.1b. For aashowerfit, there are only about ten events in the bin closest to zero degrees. For JGandalf there are 1000 events in the first bin. About 1.48 % of aashowerfit reconstructions are good and 69.4 % of JGandalf's reconstructions are. There are 719 events, JGandalf did not reconstruct at all. Counting these events as bad gives a percentage of 67.2 % good events for JGandalf. Thus the JGandalf track reconstruction will be used for all further analysis.

5.2 Removing the initial cascade reconstruction

As discussed in the description of the Belle Starr scan, Belle Starr assumes a shower at the initial reconstruction vertex. For JGandalf this is not the case, since the position vertex is where the position fit has the least error. This means it is in the center of the track most of the time. If the original code is still used to compute the likelihood, the result will be unusable.
The likelihood of such a reconstruction plotted in Figure 5.2 shows an event, where the initial shower fit was not removed. As expected, the initial shower fit adds hit residuals to a point, where there is no shower. This results in a significantly reduced likelihood. This feature is unphysical since it depends on the choice of origin and makes the background estimation harder. Therefore the initial shower fit is removed from the code.

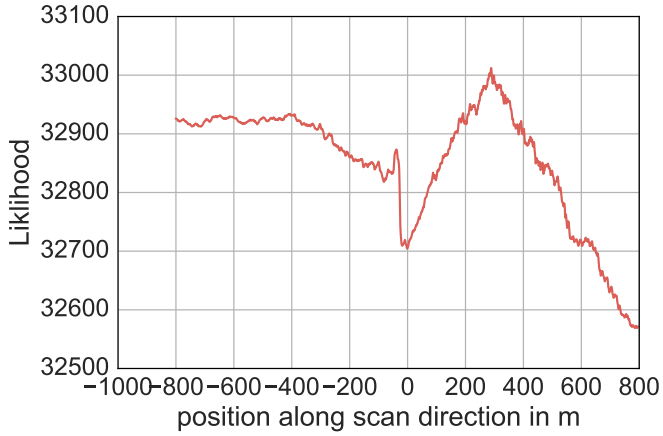

Figure 5.2: *Plot of the likelihood flip for an event when the initial shower hypothesis is not removed*

5.3 Hit merging

Another relevant point about the Belle Starr reconstruction is its hit merging before scanning. It increases the computation time, so an analysis on whether hit merging is necessary is of interest. At lower energies, hit merging does not make any difference, since there few hits arriving on one PMT within the hit merging time window. The most obvious difference is for very high energy muons.

The motivation of hit merging is the elimination of scattered light when calculating the time residuals. Scattered light from the same source arrives later than non-scattered light, so using the time of the first hit effectively removes as many effects due to scattering as possible.
There is a difference between the likelihoods calculated with and without hit merging for events with very high energies such as this muon with a reconstructed energy of 1.954 PeV in Figure 5.3. The energy may be above the range of interest, but it serves as a good example to show effects of hit merging. In the likelihood plot Figure 5.3a without hit merging, the general structure of the likelihood has more pronounced peaks, but also a more pronounced background than the likelihood plots with hit merging. With background I describe variation in the likelihood where there is no variation in the energy loss histogram. The plot with a hit merging of 10 ns in Figure 5.3b seems to add a lot of artificial structure to the background, but close significant peaks are more differentiated, for example the large double energy loss around -380 m, which is not resolved without peak merging, but is for all merging times. As the hit merging time successively increases, the structure in the background due to insignificant peaks disappears, but the resolution

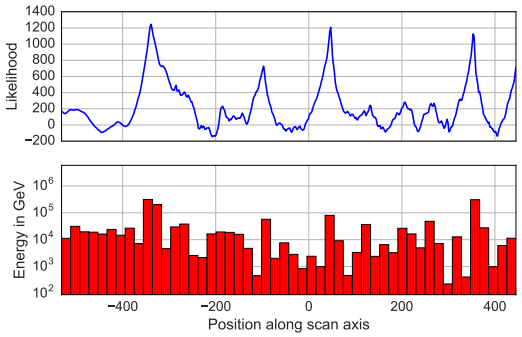

(a) *Log scale energy loss histogram and likelihood signal without hit merging*

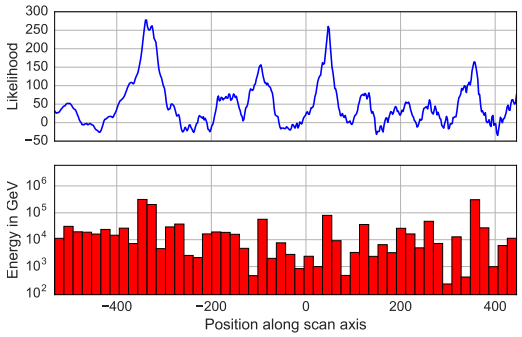

(b) *Log scale energy loss histogram and likelihood signal with hit merging of 10 ns*

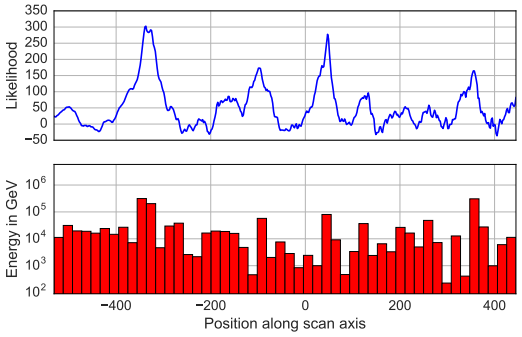

(c) *Log scale energy loss histogram and likelihood signal with hit merging of 50 ns*

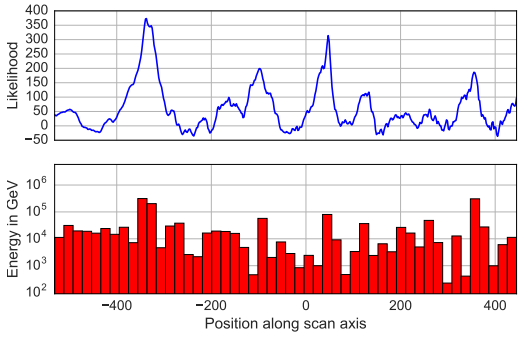

(d) *Log scale energy loss histogram and likelihood signal with hit merging of 100 ns*

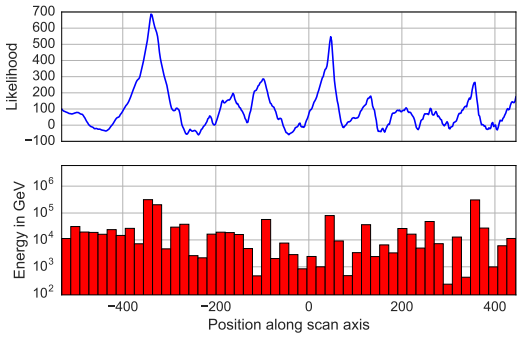

(e) *Log scale energy loss histogram and likelihood signal with hit merging of 500 ns*

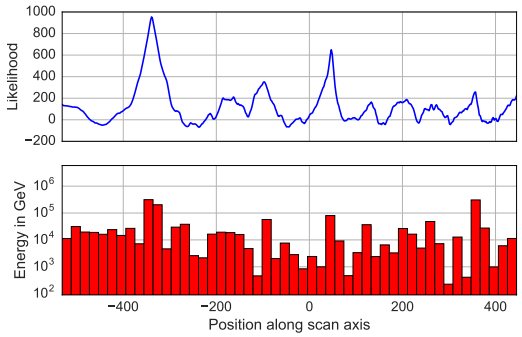

(f) *Log scale energy loss histogram and likelihood signal with hit merging of 1000 ns*

Figure 5.3: *Comparison of the Belle Starr reconstruction with different hit merging time windows for muon event with reconstructed energy of 1.954 PeV*

on significant peaks also does. For example, the resolution on the aforementioned double energy loss is worse for 1000 ns hit merging than for a 10 ns time window. So the choice

of hit merging time window is a compromise between background reduction and peak resolution. Standard values used are 300 ns for aashowerfit and 500 ns for Belle Starr. I will continue to use the 500 ns chosen for Belle Starr since it provides a reasonable compromise.

5.4 Miscellaneous changes

I have also performed other changes on Belle Starr without the motivation of the new method working better. The single event plots use a different implementation of Belle Starr in Python which allowed for more rapid single event analysis. The main difference between the original implementation and mine are the background estimation and peak detection algorithms for which I used common libraries in Python.

Instead of the background estimation built into the TSpectrum ROOT class, the asymmetric least squares (als) smoothing described in [Pen10] was used. There exist slight differences between the background estimation results as presented in Figure 5.4.

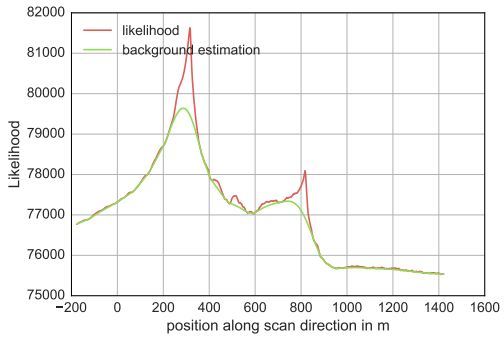

(a) *Background estimation produced for a given likelihood by the TSpectrum class*

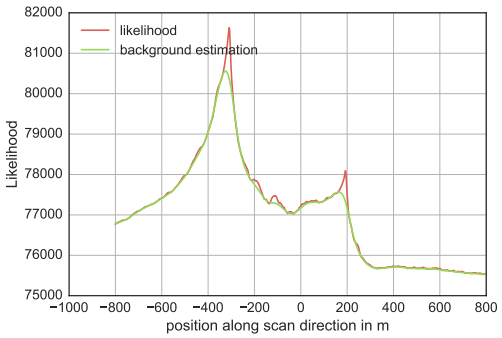

(b) *Background estimation produced for a given likelihood by the als algorithm*

Figure 5.4: *Comparison of the background estimation procedures used in the original and my own implementation of Belle Starr*

The main difference is, that the als algorithm is closer to the data than the ROOT algorithm which stays below the signal more often.
I have also used different peak finders with multiple configurations. The different results including Belle Starr's original peak finding will be discussed in a later chapter. The last major change was setting the empirical time offset used in Belle Starr for tau double bang events to zero.

6 Analysis of single events

Here I will be analyzing single events and the features and correlations of reconstruction and Monte Carlo events.
To give the reader a general idea on how the reconstruction works and how PMT hits are related, the following two plots are discussed.

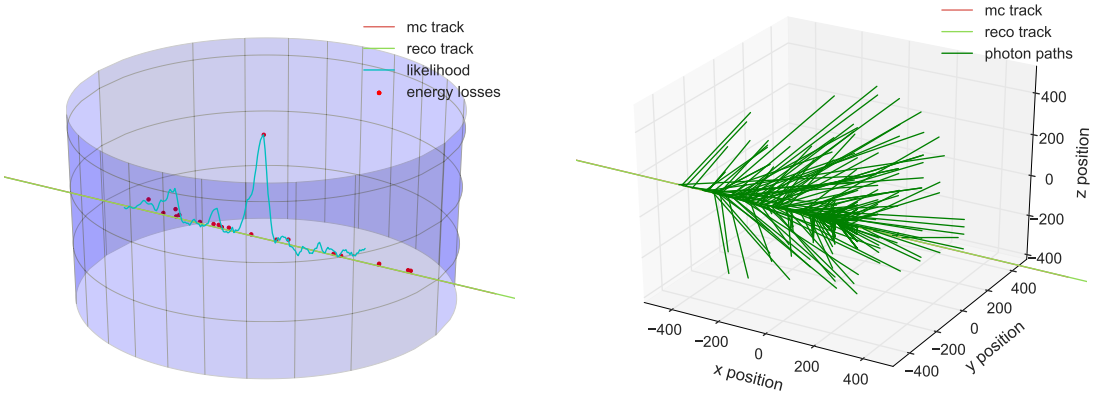

(a) *Plot of a muon track and its reconstruction including energy losses and likelihood*

(b) *Plot of a muon track and projection of all hits back onto the track with Cherenkov angle, if time residuals fit*

Figure 6.1: *Qualitative plots to illustrate the likelihood reconstruction*

In Figure 6.1a a track and its reconstruction is displayed. The corresponding likelihood function and energy loss distribution are added to the z coordinate with factors so that both fit onto the plot. Both are first normalized and then then multiplied by 500.
In Figure 6.1b, the same track is displayed. The green lines are projections from hit PMTs to the track at the Cherenkov angle in water. Then a selection on the time residuals was performed (within a 200 ns range assuming a no-scattering hypothesis). It is not entirely obvious, but the density increases in areas, where the likelihood is large and decreases, where it is not.

6.1 Neutrino events

The main analysis of single atmospheric muon events will be done with initial charged current interactions outside of the CAN. This is done to reduce secondary effects due to

the initial interaction. Antimuon neutrinos and muon neutrinos will not be differentiated in this analysis.

All events have been produced with the Python implementation of Belle Starr. The scan range is from -2000 to 2000 with a total of 2000 points resulting in one point per two meters. The scan was then reduced by a containment cut. This cut is the geometrical intersection of the scan line with the CAN volume including the surrounding are used for simulation purposes.

Discussion of Figure 6.2

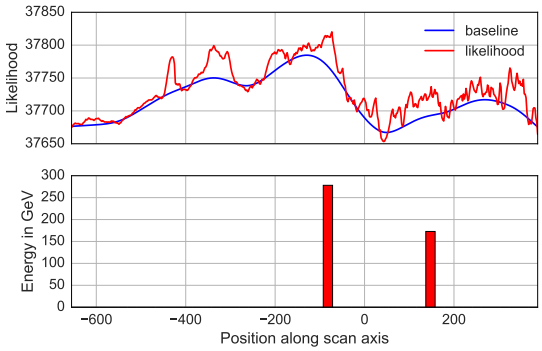

(a) *Linear scale energy histogram and likelihood including background*

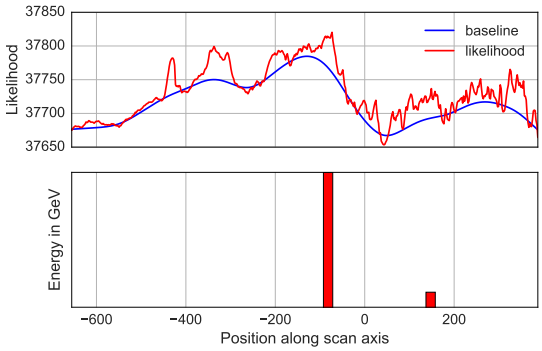

(b) *Log scale energy histogram and likelihood including background*

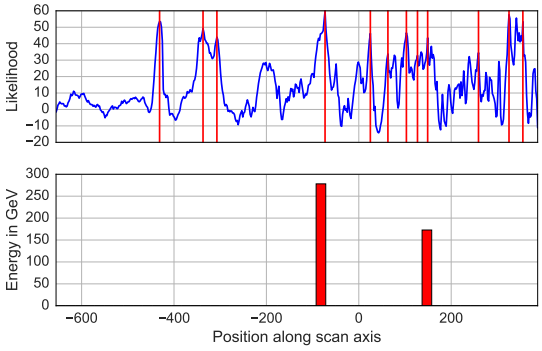

(c) *Linear scale energy histogram and likelihood without background*

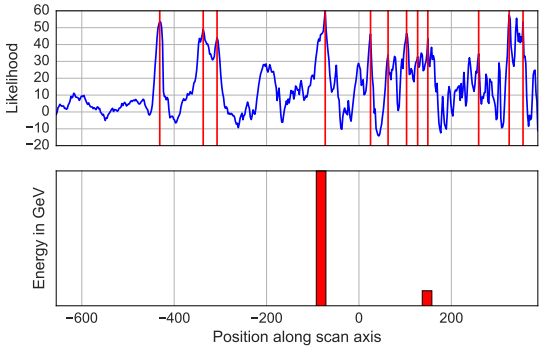

(d) *Log scale energy histogram and likelihood without background*

Figure 6.2: *Muon with 5.839 TeV of initial reconstructed energy and 500 ns hit merging time window*

E_{rec}	E_{MC}	ΔE_{MC}	$\vec{P}_x$	$\vec{P}_y$	$\vec{P}_z$	$\vec{D}_x$	$\vec{D}_y$	$\vec{D}_z$
5.8 TeV	5.0 TeV	1.9 TeV	79 m	60 m	-66 m	-0.30	-0.37	-0.87

Table 6.1: *Specifics of the muon plotted in Figure 6.2*

In Figure 6.2 and Figure 6.2 a muon with a reconstructed energy of 5.839 TeV is displayed. A hit merging of 500 ns was used in the reconstruction (implicit from now on).
In Figure 6.2a, the Monte Carlo energy loss is shown in the lower plot as a histogram. The binning is 50 bins for all following events if not explicitly stated otherwise. The statistic for the bins used is summing over all energies in the bin. The upper plot shows the result of the reconstruction in red and the estimated background in blue. The plot in Figure 6.2c has the same energy loss plot, but the upper plot shows likelihood - background, which I will call signal from now on. The figures on the right have the same top plots as the ones on the left, but the MC energy loss was plotted on a log scale. I have included duplicates in order to be able to better associate the general form of the likelihood with that of the energy loss for every plot configuration. The muon goes from the bottom right of the detector to the upper left.
The energy loss plot shows two energy loss events of 278 GeV and later 172 GeV. This is a very low energy event for a muon from a single cosmic neutrino. It is immediately clear, that the likelihood scan does not work well for particles with energies this low. The km3 simulation does not record all energy losses, just all above a certain energy threshold. So there may well be smaller energy losses not shown in the energy histogram. But there are still artifacts with significant height in the likelihood, that do not correspond to significant stochastic energy losses. For a statistical analysis, events with energies this low should be excluded to produce sensible results.

Discussion of Figure 6.3

E_{rec}	E_{MC}	ΔE_{MC}	$\vec{P}_x$	$\vec{P}_y$	$\vec{P}_z$	$\vec{D}_x$	$\vec{D}_y$	$\vec{D}_z$
29.3 TeV	33.8 TeV	16.3 TeV	-1 m	-67 m	-89 m	0.31	0.80	-0.51

Table 6.2: *Specifics of the muon plotted in Figure 6.3*

The muon in Table 6.2 is moving from the top back of the detector to the bottom front. The muon comes close to the detector center. The energy distribution has one major peak close to the middle with an energy of 7.927 TeV. The differences to the previous events are, that the particle passes through the center of the detector and has many smaller stochastic energy losses.

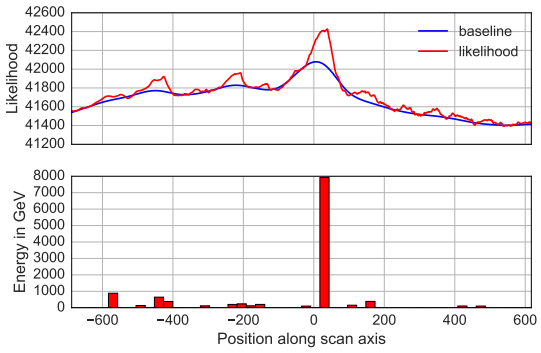

(a) *Linear scale energy histogram and likelihood including background*

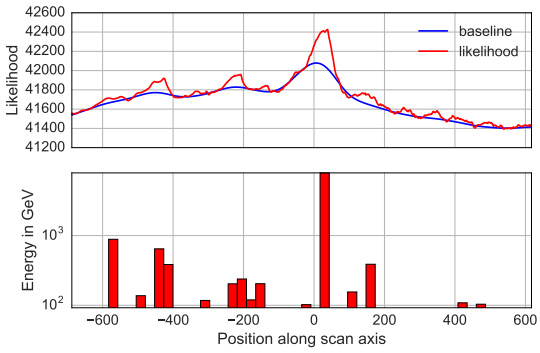

(b) *Log scale energy histogram and likelihood including background*

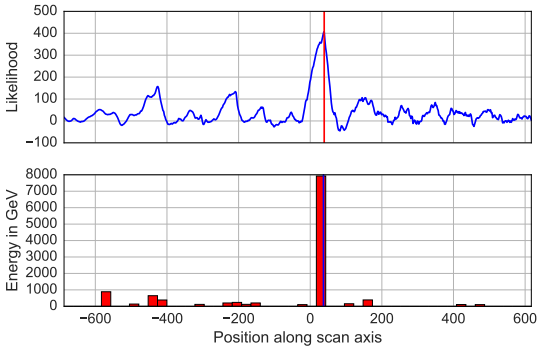

(c) *Linear scale energy histogram and likelihood without background*

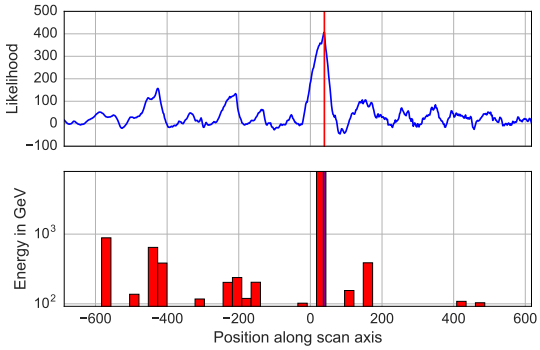

(d) *Log scale energy histogram and likelihood without background*

Figure 6.3: *Muon with 29.323 TeV of initial reconstructed energy and 500 ns hit merging time window*

The energy reconstruction is far better than the one of the last event. The likelihood also represents the physical energy loss much better. All significant energy losses show structure in the likelihood distinct from the background. I am excluding the two small peaks at the end since they are very small energy losses at the edge of the detection volume.

Up until now, a common theme has been the suppression of the likelihood with distance from the initial position vertex, which is the center of the muon track. If one were to attempt to reconstruct an energy from the likelihood without an energy fit, this has to be taken into account.

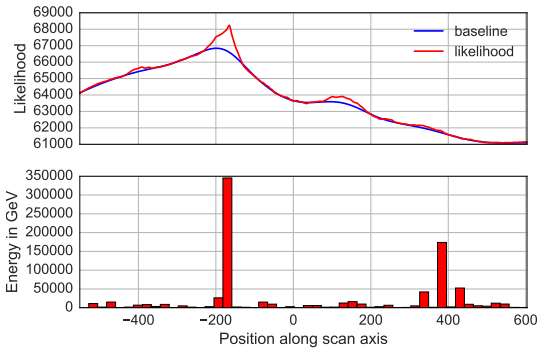

(a) *Linear scale energy histogram and likelihood including background*

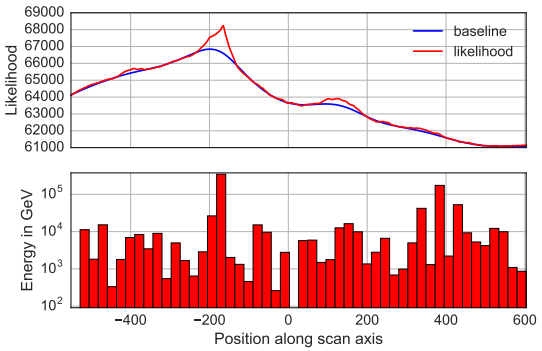

(b) *Log scale energy histogram and likelihood including background*

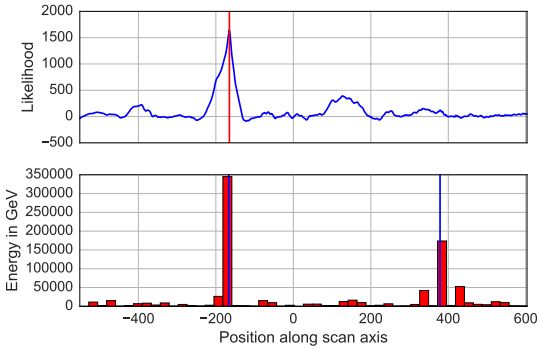

(c) *Linear scale energy histogram and likelihood without background*

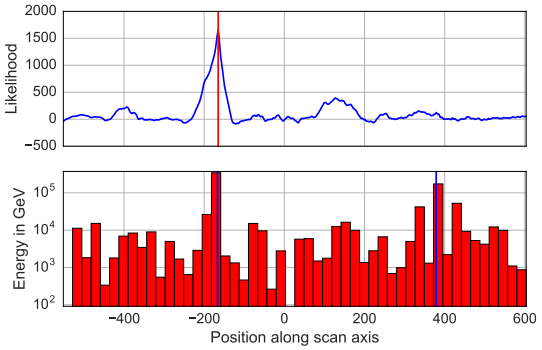

(d) *Log scale energy histogram and likelihood without background*

Figure 6.4: *Muon with 748.806 TeV of initial reconstructed energy and 500 ns hit merging time window*

Discussion of Figure 6.4

E_{rec}	E_{MC}	ΔE_{MC}	$\vec{P}_x$	$\vec{P}_y$	$\vec{P}_z$	$\vec{D}_x$	$\vec{D}_y$	$\vec{D}_z$
748.8 TeV	342.3 TeV	159.8 TeV	-110 m	153 m	31 m	0.05	-0.61	0.79

Table 6.3: *Specifics of the muon plotted in Figure 6.4*

The muon in Table 6.3 propagates from the left top of the detector through the center to the right bottom. The general structure of the likelihood is much smoother than for the previous muon tracks. This muon has two large energy losses at -200 and 400 with energies of 342.300 TeV and 159.757 TeV. The other energy losses are below 50 TeV. In general, there is a remarkable congruence between the likelihood and energy loss pattern. It is again very obvious, that the likelihood peak corresponding to the large energy loss at

400 is attenuated by being so far at the end of the muon track.

That such a pattern would emerge, is clear since photons emitted at the end of the detector have a high chance of escaping the detection volume without being detected at all. This is not the case for peaks at the beginning of the track since the photon is emitted to the front.

6.2 Atmospheric muon bundle events

There are far fewer well reconstructed muon bundle events than single high energy muon events. This is mainly due to the fact, that JGandalf was written with the latter in mind. The energies are more constrained, ranging from 10 TeV to about 50 TeV. The most interesting variable in this case is the number of muons in a bundle, so I will discuss events with different muon multiplicities.

Discussion of Figure 6.5

E_{rec}	E_{MC}	ΔE_{MC}	$\vec{P}_x$	$\vec{P}_y$	$\vec{P}_z$	$\vec{D}_x$	$\vec{D}_y$	$\vec{D}_z$
22.4 TeV	11.3 TeV	9.3 TeV	-288 m	127 m	13 m	-0.41	0.24	-0.88

Table 6.4: *Specifics of the muon plotted in Figure 6.5*

In Figure 6.5 and Table 6.4 a muon bundle with twelve muons is plotted. The muon bundle propagates from the back to the bottom front of the detector crossing the center. Let me define the lateral spread of a muon bundle at this point as $L := (\max(X_{\text{bundle}}) - \min(X_{\text{bundle}}), \max(Y_{\text{bundle}}) - \min(Y_{\text{bundle}}))$ with X_{bundle} being the set of x positions of bundle muons and Y_{bundle} the y positions. Let L_x and L_y be the components of the spread. The lateral spread for this muon track is (17.04 m, 21.29 m). The bundle energy, the sum of energies for all bundle muons, is 11.308 TeV and the total energy lost is 9.267 TeV. So the energy fit is off by a factor of two. The likelihood function actually resolves all significant energy losses, but there are far more false positives than for the high energy muon events at this energy. This is due to the pronounced background in the likelihood which stems from continuous energy loss patterns of all muons in the bundle which implies a stronger non-stochastic background.

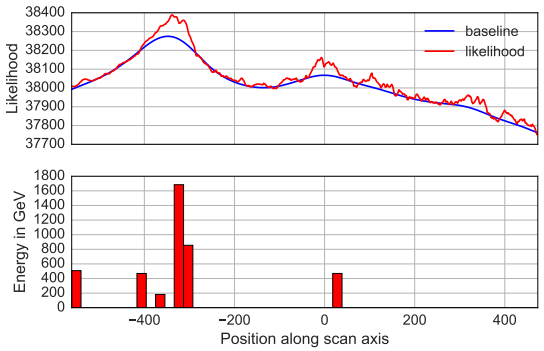

(a) *Linear scale energy histogram and likelihood including background*

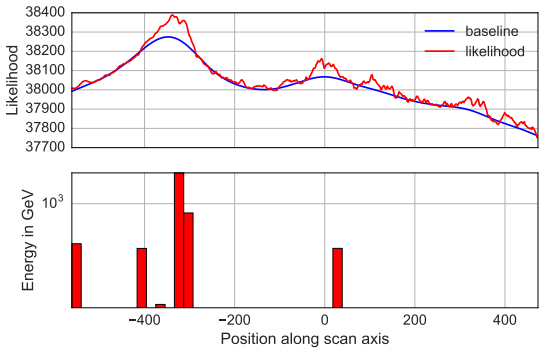

(b) *Log scale energy histogram and likelihood including background*

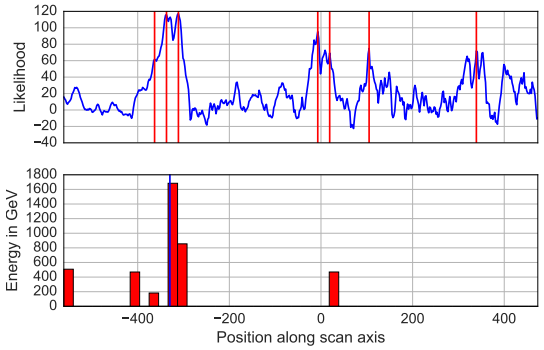

(c) *Linear scale energy histogram and likelihood without background*

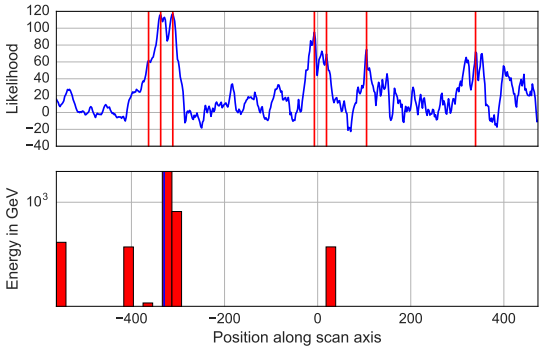

(d) *Log scale energy histogram and likelihood without background*

Figure 6.5: *Muon bundle with twelve muons and a reconstructed energy of 22.395 TeV and 500 ns hit merging time window*

Discussion of Figure 6.6

E_{rec}	E_{MC}	ΔE_{MC}	$\vec{P}_x$	$\vec{P}_y$	$\vec{P}_z$	$\vec{D}_x$	$\vec{D}_y$	$\vec{D}_z$
22.2 TeV	14.2 TeV	11.3 TeV	334 m	-21 m	-103 m	-0.36	-0.66	-0.66

Table 6.5: *Specifics of the muon plotted in Figure 6.6*

InFigure 6.6 and Table 6.5 a muon bundle with 28 muons propagates through the detector. The bundle propagates from the back of the detector a little bit below the center of the detector to the front. Just like for the last event, the energy is overestimated by a factor of about two. The lateral spread of the bundle is (35.23 m, 37.11 m) which is significantly higher as expected for this many muons. The false positives in the background are even

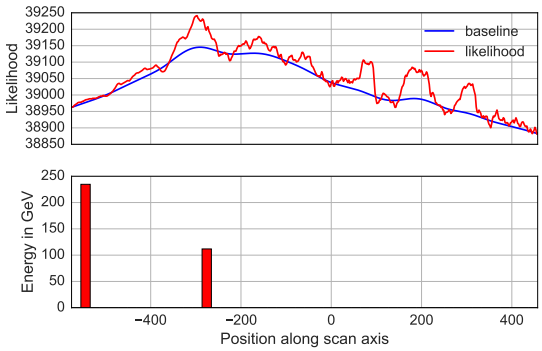

(a) *Linear scale energy histogram and likelihood including background*

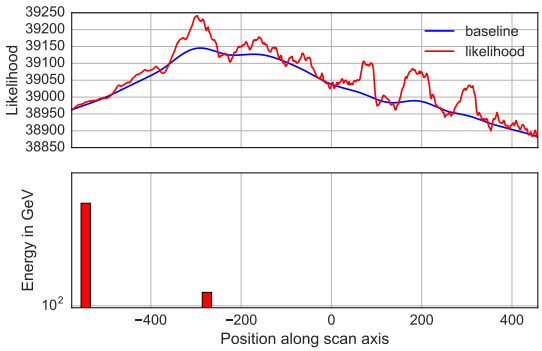

(b) *Log scale energy histogram and likelihood including background*

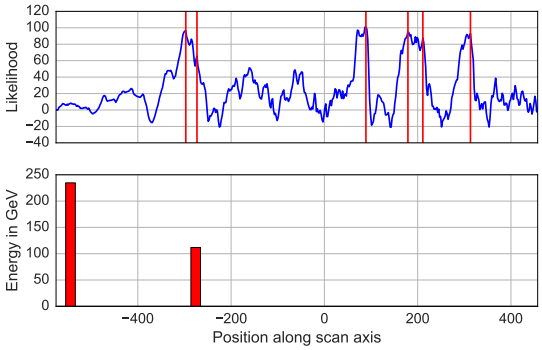

(c) *Linear scale energy histogram and likelihood without background*

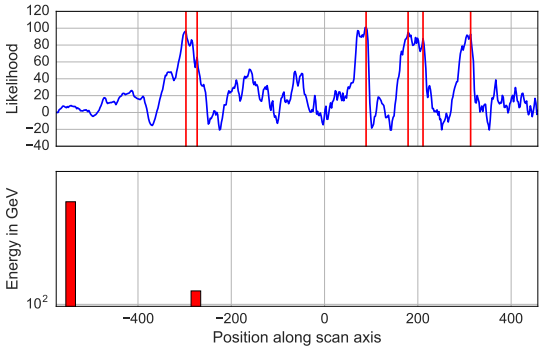

(d) *Log scale energy histogram and likelihood without background*

Figure 6.6: *Muon bundle with 28 muons and a reconstructed energy of 22.180 TeV and 500 ns hit merging time window*

stronger than in the example with less muons. This leads to the hypothesis, that the number of false positive peaks scales with the number of muons.

Discussion of Figure 6.7

E_{rec}	E_{MC}	ΔE_{MC}	$\vec{P}_x$	$\vec{P}_y$	$\vec{P}_z$	$\vec{D}_x$	$\vec{D}_y$	$\vec{D}_z$
61.5 TeV	34.2 TeV	22.2 TeV	-208 m	-205 m	-14 m	0.39	-0.35	-0.85

Table 6.6: *Specifics of the muon plotted in Figure 6.7*

To test this hypothesis for high muon numbers, the event plotted in Figure 6.7 consists of 58 bundle muons. The muon is propagating from the top left of the detector to the bottom right. The track does not pass the center of the detector but stays in front of it.

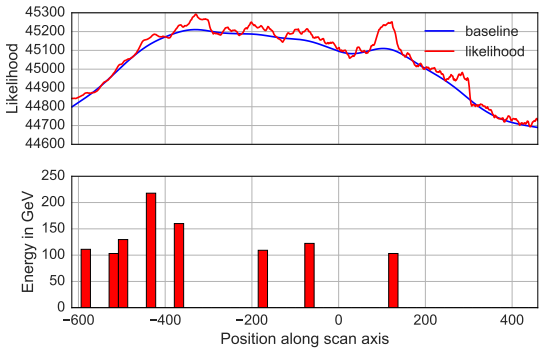

(a) *Linear scale energy histogram and likelihood including background*

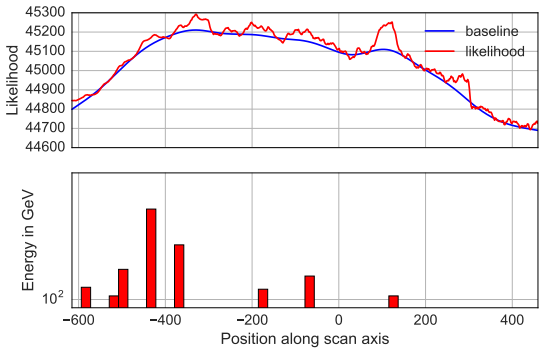

(b) *Log scale energy histogram and likelihood including background*

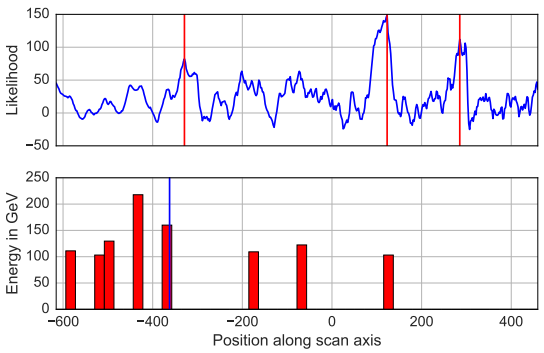

(c) *Linear scale energy histogram and likelihood without background*

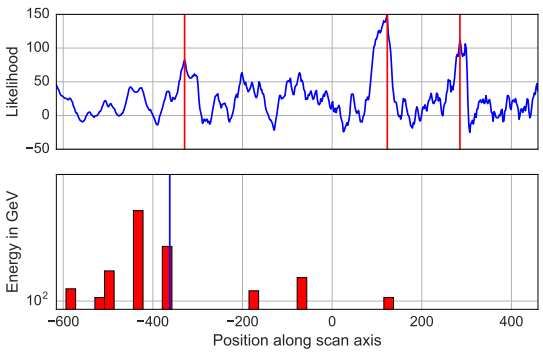

(d) *Log scale energy histogram and likelihood without background*

Figure 6.7: *Muon bundle with 58 muons and a reconstructed energy of 61.521 TeV and 500 ns hit merging time window*

The energy is overestimated by a factor of two again. The lateral spread for this muon bundle is (35.23 m, 37.11 m) which is larger than the two previous bundles.

For this likelihood, the number of false positives is reduced by a large amount. This is most likely since some of the background, which triggered the false positives before now passes the energy threshold for a stochastic energy loss since there are so many muons in the bundle.

7 Statistical analysis of many events

After talking about single events in detail and formulating some hypotheses it is time to test them by means of statistical analysis on a large set of events. Unless specifically mentioned, the discussion will concern high energy single muon events. The events used are shown in Table 7.2.

7.1 Justification and description of quality cuts

In the analysis of the events, I have used several cuts to ensure the quality of the reconstructed tracks. I will now show several plots justifying these cuts. The cuts used were .

Cut name	Implementation
Radial cut	$r_{\text{event}} < 506.21$
Z component cut	$-405.93 < z_{\text{event}} < 508.68$ (**None**)
JGandalf likelihood cut	$-L_{\text{Gandalf}} > -200$
JGandalf normalized likelihood cut	$-L_{\text{red}} > -0.4$
β_0 cut	$\beta_0 < 0.003$
β_1 cut	$\beta_1 < 0.003$
Energy cut	$3 * 10^3 < E_{\text{Gandalf}}$

Table 7.1: *Description of quality cuts employed in the selection of events to be used for further evaluation*

With the previous definition of good event and bad event, the following histograms display the distribution of the two depending on the listed quality parameters. Good events are green, bad ones are red. The histograms are stacked.

Geometrical containment cuts

The plots in Figure 7.1 show, how relevant containment of the largest likelihood position in the detector is for the reconstruction.

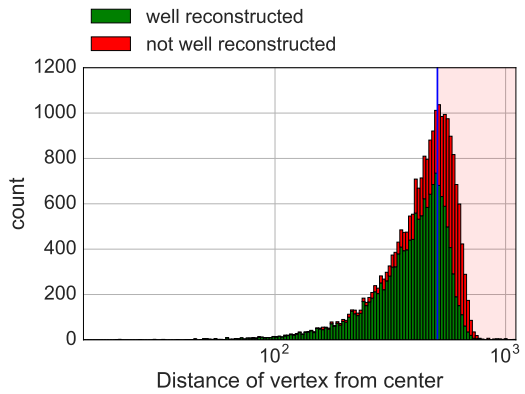

(a) *Histogram and quality cut for the distance of the largest likelihood in the reconstructed track from center*

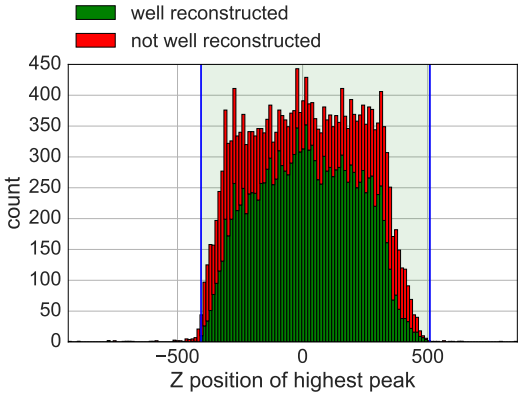

(b) *Histogram and quality cut for the z component of largest likelihood position in the reconstructed track from center*

Figure 7.1: *Geometrical containment cuts used to determine quality of track*

The z position plotted on the x axis of Figure 7.1b is the z component of the reconstructed position of the largest likelihood. The distance from the center in Figure 7.1a is the distance of the largest likelihood veretex from the detector center, which is the origin by definition.
In both plots, the track behavior is as expected. The further out the largest likelihood and presumably the largest energy loss, the worse the reconstruction. For a more sophisticated cut, the direction of the particle should also be considered since a large energy loss for an outgoing particle is going to yield less information than for an ingoing particle due to the long absorption and scattering lengths for visible light.
I set the cut for the radial containment to 300 m in order to keep as many good events as possible while rejecting as many bad events as possible. Since the distribution in z direction is symmetric, the radial cut suffices. Thus the z position cut is set above the radial cut to the detector volume. Had there been strong asymmetries, then an implementation of a cut for the z position would have made sense.

JGandalf likelihood cuts

In Figure 7.2 both likelihoods provided by JGandalf are plotted against the good event/bad event distribution.
Since the likelihood in Figure 7.2b is a histogram plotted on a log scale, I have taken its absolute value. The value of the likelihood is usually negative.
Both likelihoods are good parameters for the quality of the reconstruction.
The quality cut for the raw likelihood Figure 7.2b is set to -200 in order to eliminate the peak of bad events around 10^2. The quality cut of the reduced likelihood is more conservative with -0.5 since there are no major peaks of bad events.

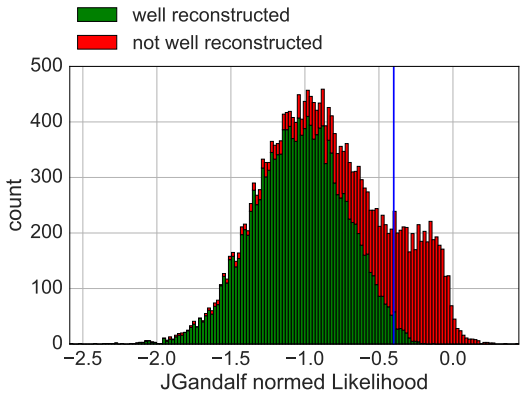

(a) *Histogram and quality cut for the normalized likelihood from JGandalf*

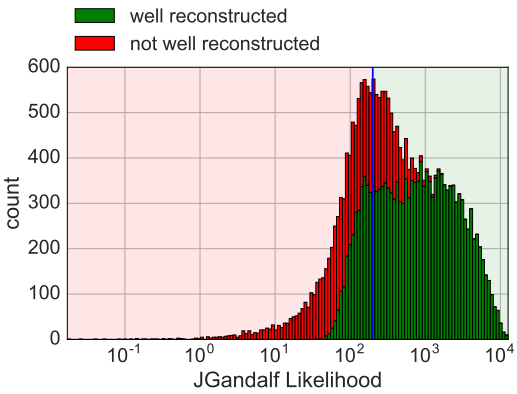

(b) *Histogram and quality cut for the likelihood from JGandalf*

Figure 7.2: *JGandalf likelihood cuts used to determine quality of track*

JGandalf β parameter cuts

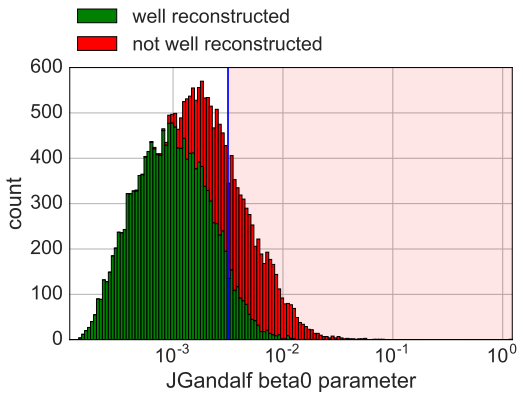

(a) *Histogram and quality cut for β_0 provided by JGandalf*

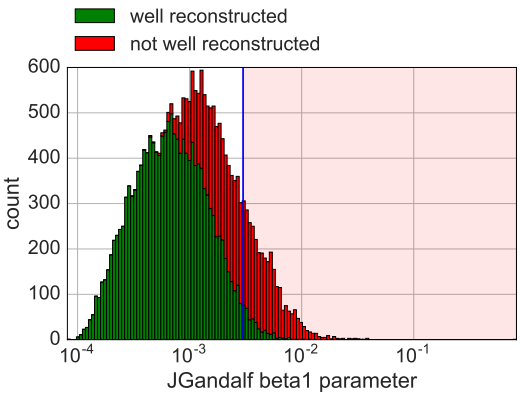

(b) *Histogram and quality cut for β_1 provided by JGandalf*

Figure 7.3: *JGandalf uncertainty cuts used to determine quality of track*

InFigure 7.3 the β parameters from the JGandalf reconstruction are plotted. Thus mainly the direction of the reconstructed tracks should be affected by the used cuts.

The β_0 parameter in Figure 7.3a and the β_1 parameter in Figure 7.3b both depend on the same quantities, the uncertainties in the direction cosines.

So it is reasonable, that both plots look almost identical. The cuts for β_0 and β_1 were both set to 0.003. It is very likely, that the intersection of removed events is very large due to this.

Energy cut

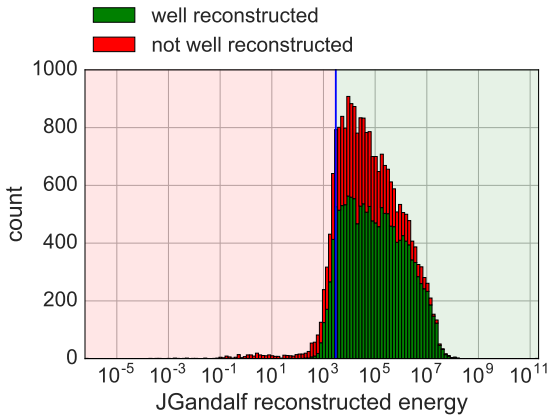

Figure 7.4: *Histogram and quality cut for the reconstructed track Energy*

In Figure 7.4, the cut on the reconstructed particle energy is shown.

There does not seem to be any major correlation between the energy and the good event/bad event distribution, although one might expect the reconstruction to be bad for energies to low or too high.

Still, there are implemented cuts for the energy. This is due to the previous observation, that the likelihood produced by the Belle Starr scan is worse for particles with low energies. Since there is currently no measure on how the energy will affect the energy loss vertex reconstruction, the cut has been set to 3 TeV since the detector is most sensitive between 1 TeV and 1 PeV. There was a cut on the distance between the two largest likelihoods for the tau double bang reconstruction, but it no longer makes physical sense in case of a muon track reconstruction.

7.2 Reconstruction after quality cuts

After implementing these quality cuts, I examine how well they worked by discussing the differences between the reconstruction and the MC truth. Here, one more quality parameter than for the comparison between the JGandalf and aashowerfit reconstruction is used. This parameter is the distance of the largest likelihood from the MC track (the length of the orthogonal projection vector of the point onto the track). A total of 97 % of events, that pass quality cuts are good events. In Table 7.2, the exact distribution of event types is shown. In can events are events with the initial interaction inside the CAN and outside of CAN events the opposite.

type	quality cuts	number of events
All	No	22600
$\bar{\nu}$ In CAN	No	4995
$\bar{\nu}$ Outside of CAN	No	5941
ν In CAN	No	5057
ν Outside of CAN	No	6607
All	Yes	8648
$\bar{\nu}$ In CAN	Yes	1765
$\bar{\nu}$ Outside of CAN	Yes	2433
ν In CAN	Yes	1708
ν Outside of CAN	Yes	2742

Table 7.2: *Table of the distribution of the simulated events used in data analysis*

So about $\frac{1}{3}$ of the total events are left after quality cuts and in CAN events are affected more than events with the initial interaction outside of the CAN. There is no significant difference between ν and $\bar{\nu}$. It should be noted, that these are all events, where the neutrino was forced to interact to produce a muon.

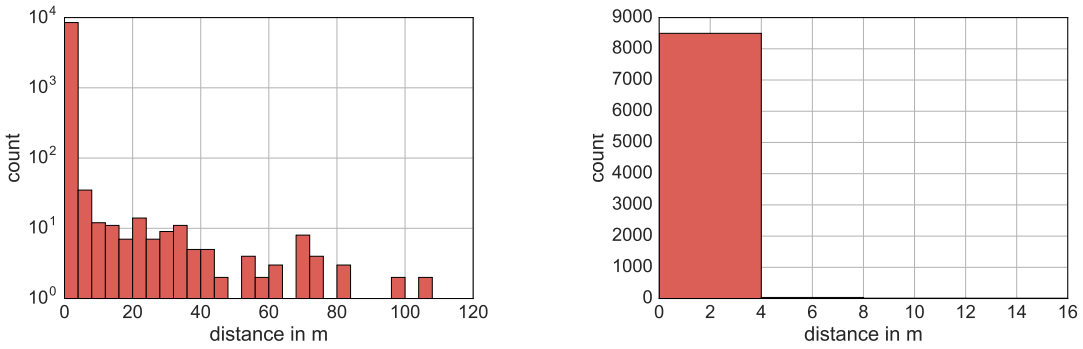

Figure 7.5: *Histograms for the distribution of geometrical distance of the MC track from the vertex reconstruction over the full range. The log plot is on the left and the linear plot on the right.*

For a range of 160 m and a bin number of 50, the size of a single bin is 3.2 m in Figure 7.5. So every event collected in the first bin is a good event and it is especially clear in the linear plot, that this bin is the largest with almost 9000 events in it, whereas all other bins have a content well below 100, which can be seen in the logarithmic plot. A total of

98.2 % of events, that passed the quality cuts also have a minimal distance smaller than 4 m.

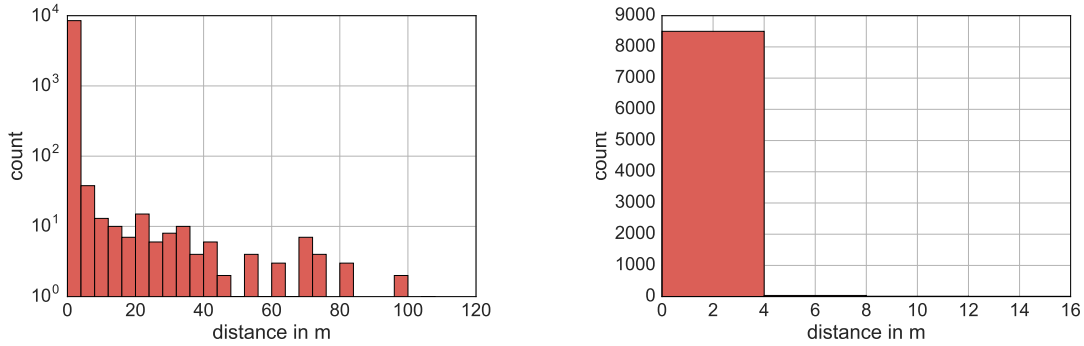

Figure 7.6: *Histograms for the distribution of geometrical distance of the MC track from the highest likelihood vertex reconstruction over the full range. Left is the log plot and right the linear plot.*

The plots in Figure 7.6 are similar to the plots discussed previously. This makes sense, since the angles between reconstructed tracks which pass quality cuts and MC tracks are very small. If a given reconstruction vertex deviates by some amount from the MC track and the angle between the two tracks is small, any point on the reconstructed track will not be far from the MC track since the detection volume is bounded. This histogram is positively influenced by the cuts performed on the reconstructed position with the highest likelihood.

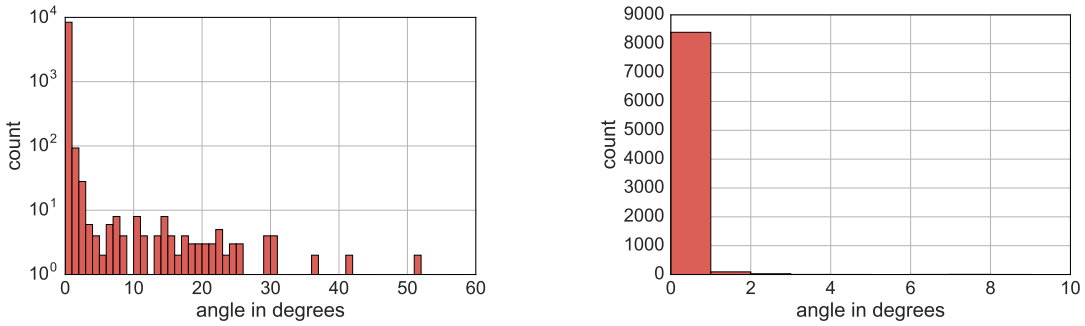

Figure 7.7: *Histogram for the distribution of angles in degrees between the MC track and the reconstructed track over the full range. Left is the log plot and right the linear plot.*

The binning in Figure 7.7 has been chosen such that one bin corresponds to one degree. So every event in the first bin is a good event. As it was for the plots for the reconstructed vertex distances from the MC track, the first bin has far more content than the other bins. A little more than 8000 events are in the bin corresponding to good events. This is

less than for the position plots and yields a percentage of 97.1% of the remaining events, which also pass the angular criterion for good events.

7.3 Energy loss - likelihood analysis

This section is dedicated to the reconstruction of cascade positions and their energy with Belle Starr.

7.3.1 Cascade identification

The main goal of this analysis is the identification of cascade positions. This is the parameter, that should be well reconstructed. There might be a correlation between the likelihood and the energy, but it must not necessarily exist. To find out, how well cascades were reconstructed, I try to correlate peaks in the energy loss distribution with ones in the likelihood function. This is done by forming the Cartesian product between the two sets and then removing the pair with the smallest distance between them. These two peaks are then called correlated. All pairs including either of the two peaks in the correlated peak just found are also removed from the set. This construction is applied recursively until the set is empty. If the number of peaks for the two distributions is not equal, there can be peaks which are not part of a pair of correlated peaks.
Quality parameters for the position reconstruction of the cascade vertices are the distance between two correlated peaks and the difference between the number of peaks found in the energy spectrum and the likelihood spectrum. The definition of the origin has been changed for this peak analysis to highlight systematic effects. It is now the point of entry for the muon for outside of CAN events. For an in CAN event, it is the initial interaction vertex.

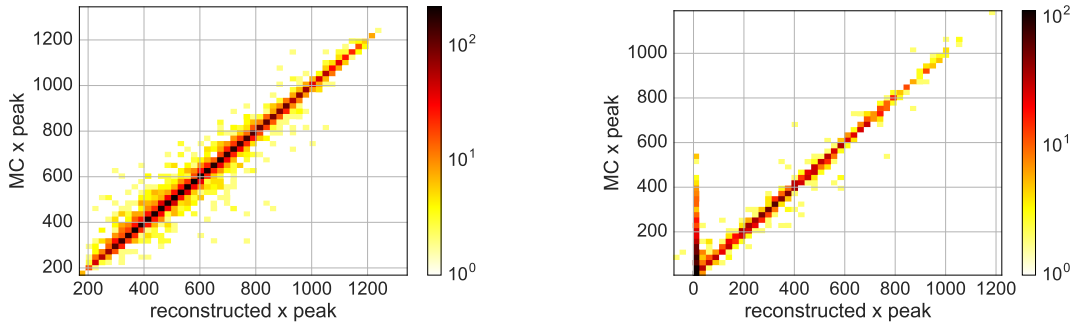

Figure 7.8: *x position of reconstruction and MC track. Out of CAN left and in CAN right*

Events with a very small deviation from the origin in reconstructed position are systematically associated with the wrong peak. This is due to the likelihood reconstructing the

initial interaction for in CAN events as can be seen in the plots in Figure 7.8, whereas there is no indication in the energy losses since it is by definition the spectrum of photons emitted by the muon and not produced in the initial interaction.

There are three different methods I used for background estimation and peak finding which are combinations of two different peak finders and two different baseline estimations. The baseline estimation has already been discussed previously. There is the ROOT class TSpectrum, which I will denote with background R and the als baseline in Python, I will denote with background N. For the peak finder, there are the ROOT TSpectrum class's algorithm, I will denote with peak finding R. The implementation used in Python is from the package peakutils which is a very simple peak finding utility based on the first derivative and the first order differences of the data. I will denote the usage of this method with peak finding N.

Background estimation N and peak finding R

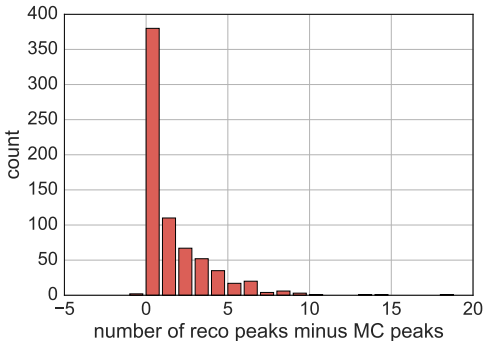

(a) *The difference between reconstructed peak and MC peak number*

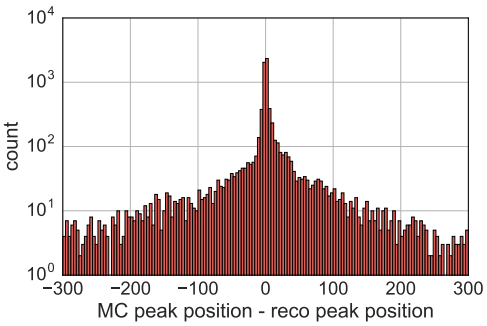

(b) *Histogram of position difference along the scan direction for MC position minus reconstruction position*

Figure 7.9: *Position reconstruction for the background calculation N and the peak finding R*

Displayed in Figure 7.9 are the results for using the background estimation R and the peak finding method N. The parameters used for the peak finder and the background estimator were found by examining their sensibility on single events.
In Figure 7.9a, the number of peaks found for MC energy loss was subtracted from the number of peaks found for the reconstructed likelihood. The largest bin is the one containing events with the same amount of peaks for both. Most other events are in bins on the right of the zero bin indicating, that this method prefers false positives to peaks not found.

Figure 7.9b shows a histogram of the position of the MC vertex minus the position of the reconstruction vertex for a correlated peak. The bins are chosen such that the two bins are 4 m in width. This means, that all events in the two bins closest to zero are well reconstructed in position. However these bins would also hold the largest number of events for a random distribution of peaks due to the definition of correlated peaks.
So as check for this, the mean and median for the correlated peak distances were also calculated for peaks with random positions along the track, but the same number of peaks as the real data. The median of the real data is 2.99 and the mean of it is 35.57 and the number of peaks per event is 0.96. The median of the random data is 42.63 and the mean is 87.54. First, the reconstruction's resolution is well above random noise. Second, the median of the real data is far smaller than the mean, which is to be expected since the mean weights bad events more than good events.

Background estimation N and peak finding N

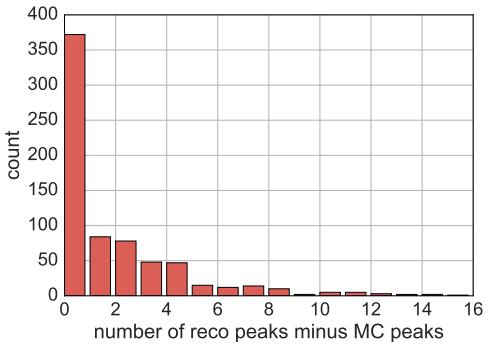

(a) *The difference between reconstructed peak and MC peak number*

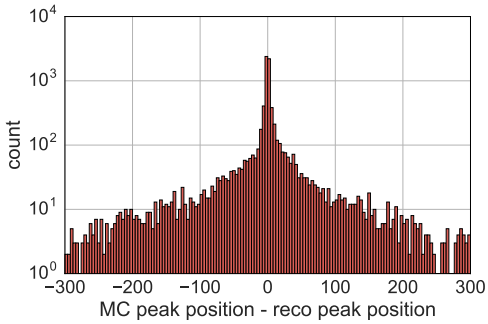

(b) *Histogram of position difference along the scan direction for MC position minus reconstruction position*

Figure 7.10: *Position reconstruction for the background calculation N and the peak finding N*

Displayed in Figure 7.10 are the results for using the background estimation N and the peak finding method N. The data axes are the exactly same as for the last discussion.
In Figure 7.10a the difference between the number of reconstruction peaks and MC peaks has the largest bin at zero with about 380 events. The other bins with significant contributions are to the right indicating that there are false positives in the likelihood peak identification. This is done so that they can be excluded with a cascade energy fit later. The other bins are smaller by a factor of three or more. The difference between the number of reconstruction peaks and MC peaks has a similar form to the last one in Figure 7.9a. Especially the content of the first bin is almost the same. The contributions

to the bins to the right however is much flatter. This indicates, that the number of peaks is better reconstructed with the combination peak finding N and background N.
The histogram of distances in Figure 7.10b looks very similar to the one in Figure 7.9b. The median of peak distances is 2.99, the mean in 35.57 and the number of peaks per event is 0.98. So apart from the fact, that the peak finding for the likelihood is more liberal, there is no major difference between the two methods discussed so far.

Background estimation R and peak finding R

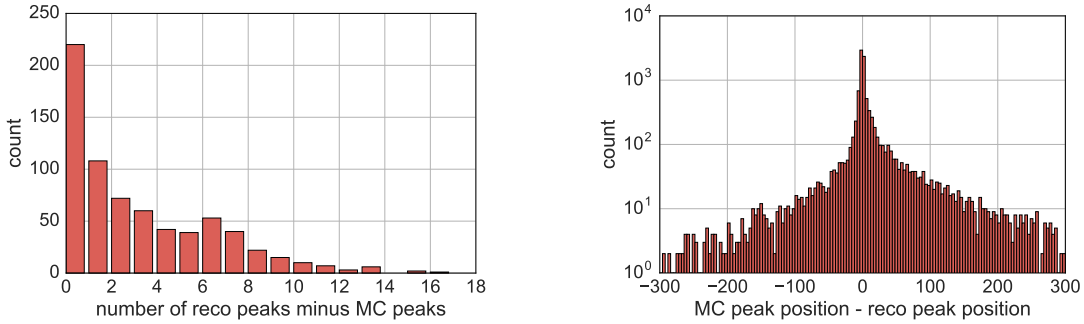

(a) *The difference between reconstructed peak and MC peak number*

(b) *Histogram of position difference along the scan direction for MC position minus reconstruction position*

Figure 7.11: *Position reconstruction for the background calculation R and the peak finding R*

Displayed in Figure 7.11 are the results for using the background estimation R and the peak finding method R. Both distributions look significantly different to the previous ones.
The difference between the number of reconstruction peaks and MC peaks looks different to the other two variations of peak finding and background estimation. The bin for no difference in Figure 7.11a, the zero bin, has much lower content. There are no bins to the left of the origin and the bins to the right do not decrease significantly until the bin for the difference six. For an estimation of the number of peaks in the energy loss distribution this combination is the worst. However, the peak finding algorithm was also not optimized for these types of tracks, whereas the other ones were. So by changing the parameters of either the energy peak finding or the likelihood peak finding, one might find that this method works significantly better.

The distribution of peak distances in Figure 7.11b looks similar to the previous two scaled by the additional number of peaks found. An interesting difference is the fact, that peaks are more likely to be reconstructed in front of the MC vertices in this case, whereas the

opposite was true for the other peak/background combinations. The median for peak distances is 3.14 and the mean is 23.78. The number of peaks per event is 1.11. Here we can see a major difference between the medians. This cascade reconstruction has far less outliers than the other two due to its increased number of total peaks found in the reconstruction.

Energy dependence

The single plots showed, that low energy events have many false positive peaks in the likelihood. So one would expect a strong relation between the vertex reconstruction quality and the reconstructed particle energy. This relation is plotted in Figure 7.12.

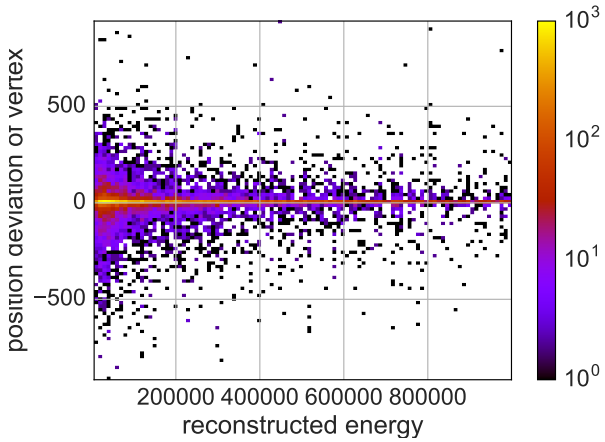

Figure 7.12: *Heatmap of the reconstructed particle energy against the vertex position difference for all reconstruction combinations.*

The relation is clearly visible. The reconstruction works fairly well for high energy particles, but fails for low energies. This is most likely due to the reasons discussed for individual events in chapter 6.

7.3.2 Energy estimation

The way in which Belle Starr usually computes its likelihood, disregarding the number of hits merged, puts a natural restriction on any attempt at energy reconstruction. Here I will investigate relations between the likelihood and the energy regardless. This reconstruction attempt is only concerned with large stochastic energy losses resulting in peaks in the energy and likelihood.
Since it is not entirely clear, whether the total likelihood without background subtraction in Figure 7.13a or the likelihood including background subtraction in Figure 7.13b is more easily mathematically related to the energy of the peak, both have been plotted.

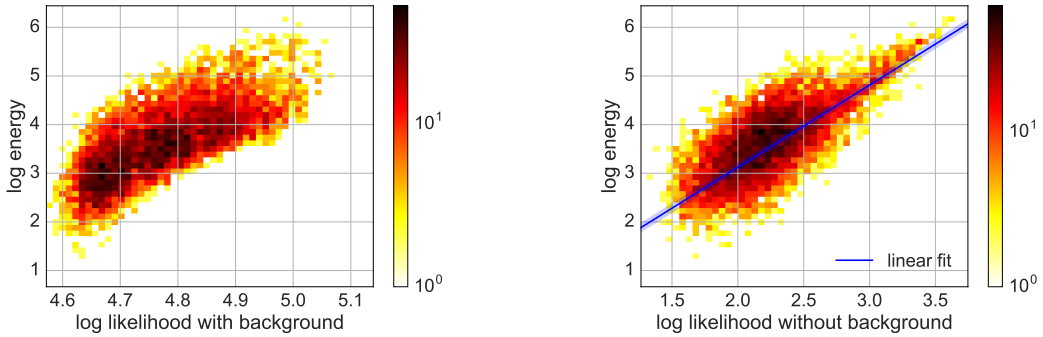

(a) *With background*

(b) *Without background for selected hits with linear fit to logarithms of likelihood and energy*

Figure 7.13: *Relation between energy and likelihood for background R and peak finding R*

Peaks with higher energy losses should be resolved better and with higher likelihood. The behavior of the raw likelihood does not change a lot over its energy and likelihood range, but the distribution of likelihood minus background versus energy does. For higher energies and likelihoods, the points tend to be less scattered than for lower energies and likelihoods. Thus the background reduced likelihood will be used for energy estimation. Of course this means, that the deduced relations strongly depend on the details of the background reduction used.

Especially for higher values of the likelihood, the relationship on the double logarithmic plot looks linear indicating a power law. The slope of the fitted line is 1.687 and the interception is -0.249 resulting in the power law:

$$E(\mathcal{L}) = 0.564 \times \mathcal{L}^{1.687} \tag{7.1}$$

In Figure 7.14a and Figure 7.14b the background reduced likelihood is used with the same reasoning as before.
The slope of the fitted line is 2.35 and the interception is -2.088 resulting in the power law:

$$E(\mathcal{L}) = 0.008 \times \mathcal{L}^{2.35} \tag{7.2}$$

In Figure 7.15a and Figure 7.15b the background reduced likelihood is used with the same reasoning as before.
The slope of the fitted line is 2.49 and the interception is -1.981 resulting in the power law:

$$E(\mathcal{L}) = 0.01 \times \mathcal{L}^{2.49} \tag{7.3}$$

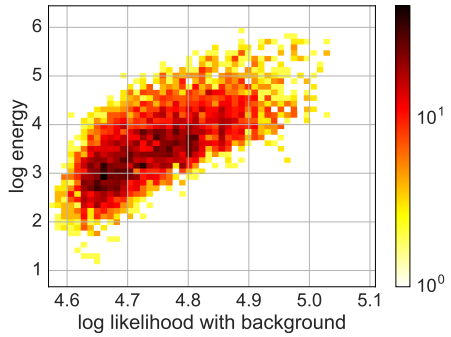

(a) *With background*

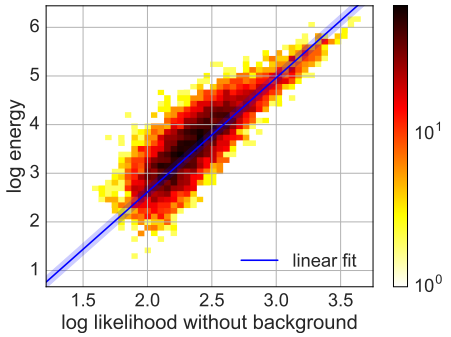

(b) *Without background for selected hits with linear fit to logarithms of likelihood and energy*

Figure 7.14: *Relation between energy and likelihood for background R and peak finding N*

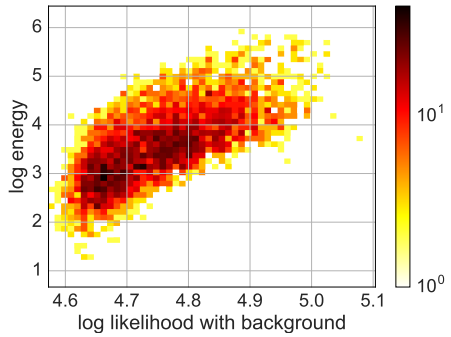

(a) *With background*

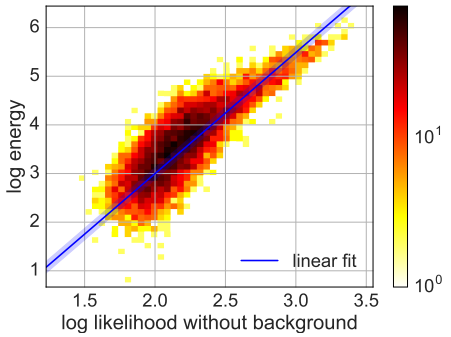

(b) *Without background for selected hits with linear fit to logarithms of likelihood and energy*

Figure 7.15: *Relation between energy and likelihood for background N and peak finding N*

Although this relationship is fulfilled to some degree, the energy estimation is lacking. Therefore one should first perform the position fit in the manner presented and then perform an energy fit at the position of the cascade. Another option is a scan with energy fits at every scan position and reduce the resolution of the scan.

8 Characterization of muon bundle and neutrino events

Using the results of the reconstruction performed on single high energy muon files and muon bundle files, the aim is to distinguish the two by characteristics in the likelihood function. There are many possible variables, that could be defined to characterize events, so I will focus on two in particular. There are also properties, which are not related to the likelihood which can differentiate the two event types.
All these investigations have been performed after applying the quality cuts discussed previously. The remaining number of neutrino events is 5645 and the remaining number of muon bundle events is 4770. The distribution of the number of muons in a bundle is plotted in Figure 8.1.

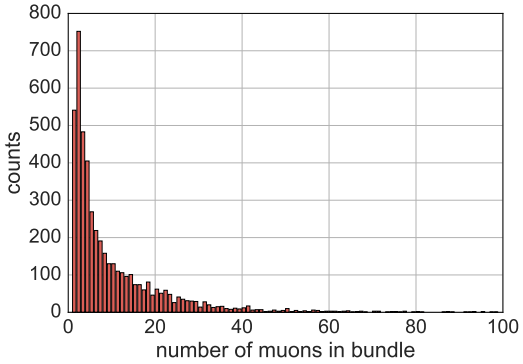

Figure 8.1: *Bar diagram for the number of muons in a bundle for all events analyzed in the following*

The largest contribution is from events with 2 muons. Depending on the energy distribution between the muons, it might be difficult to differentiate between single muon events and muon bundle events with few muons. It will be impossible to differentiate single atmospheric muons from muons from neutrino interactions with properties of the likelihood function. With 541 out of 4770 events, single atmospheric muons are a significant contribution.

8.1 Event properties not related to likelihood

First, I will shortly discuss two cuts already implemented to veto muon bundle events. In general all cuts discussed will immediately be applied in order to eliminate correlations between characterization parameters.

z component of direction vector

Since atmospheric muons stem from extensive atmospheric showers and can not cross the earth below the detector without decaying, the z component for direction vectors of muon bundles is always negative. So an upgoing muon event must necessarily be due to a neutrino interaction.

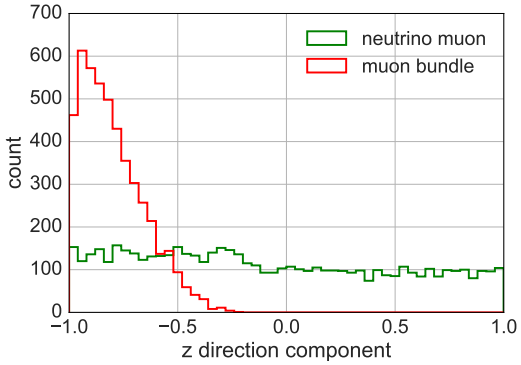

Figure 8.2: *Histogram of the z direction component of reconstructed tracks for single muons and muon bundles*

As expected, the plot Figure 8.2 shows exactly the relation discussed. Since the horizon is not at an angle of zero, even events above -0.3 are rare.

	neutrino muons	atmospheric muons
Events kept	2390	4763
Events sorted out	3255	7

Table 8.1: *A table of the groups resulting from the criterion, that the z direction be below -0.3*

In this step and in future steps, events are divided into two groups. The "sorted out" which should only contain muon neutrino in the end events and the "kept" group which only contains atmospheric muon events. The table Table 8.1 shows, that the direction of the muon can be used to sort out more than half of the neutrino muons while making

barely any error for the atmospheric muon events. This characteristic is already well known and the events are only sorted out in order to eliminate side effects due to the direction of the initial neutrino for the following discussion.

Number of hits after hit residual filtering

With the hit residual filter used for the direction and energy fit the filtered hits should correspond to the muon or muon bundle of interest. Of course this number of hits is also related to the quality of the time and direction reconstruction. This reconstruction tends to be worse for muon bundle events. The number of hits is intimately related to the reconstructed energy. The reason for choosing the number of hits instead of the energy reconstruction is that the number of hits does not rely as strongly on the quality of the reconstruction as the reconstructed energy.

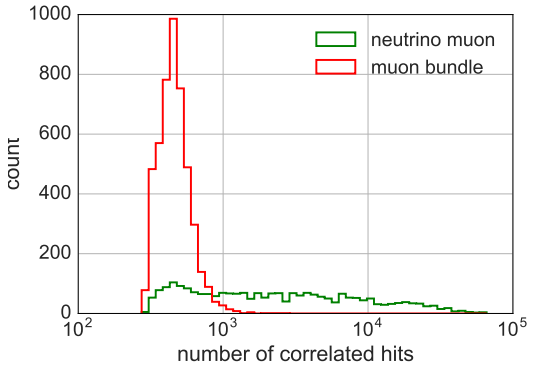

Figure 8.3: *Histogram of the hits related to reconstructed tracks for single muons and muon bundles*

As expected, Figure 8.3 shows a clear correlation between number of peaks and event type. This is simply caused by the different energy ranges of atmospheric muons and muons due to neutrino interactions. The plot from the theory section in Figure 3.4 shows, that atmospheric muons rarely exceed energies of 1 TeV. With the maximal muon number in a bundle being around 60, this sets a natural bound of about 60 TeV for atmospheric muon bundles. Energies above 100 TeV are not uncommon for muons from neutrino interactions.

	neutrino muons	atmospheric muons
Events kept	909	4748
Events sorted out	1481	0

Table 8.2: *A table of the groups resulting from the criterion, that the number of hits be in the interval [250, 1200]*

The cut on the number of hits amounting to an energy restriction shown in Table 8.2 sorts out most of the muons from neutrino interactions. It should be noted, that the lower bound on the muon bundle energy has an affect on this cut. But in this case, the cut on the number of hits is implemented in order to exclude effects in the likelihood function due to the energy dependence which is already taken care of.

JGandalf likelihood

The JGandalf reconstruction was written for muons from neutrino interactions and not bundles. So one would expect the likelihood to be worse for bundle events or at the very least, that very well reconstructed events are single muon events.

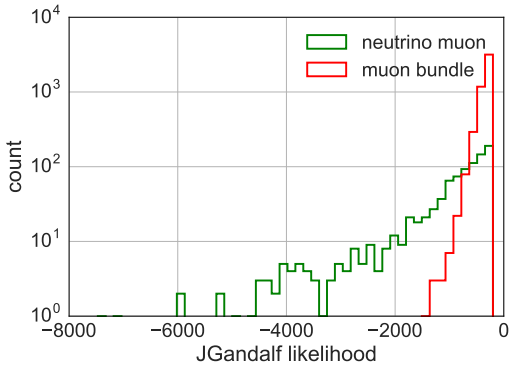

Figure 8.4: *Histogram of the JGandalf likelihood for single muons and muon bundles*

The histogram in Figure 8.4 shows, that events with very small likelihoods are muons from neutrino interactions. With the given dataset, any event with a likelihood below -1200 is one.

	neutrino muons	atmospheric muons
Events kept	713	4744
Events sorted out	196	4

Table 8.3: *A table of the groups resulting from the criterion, that the JGandalf likelihood be above -1200*

In the Table 8.3 the results of the discussed cut parameter implementation are discussed. This parameter sorts out far fewer events and a lower percentage than the last two, but the error made for atmospheric muons is low with four events out of 4774.

8.2 Properties of the event's likelihood

This section includes a discussion of properties based on the event's reconstructed likelihood function.

Variation

First define the variation of a function as the standard deviation of the distances between adjacent points. If the variation of an event is larger, one would expect its energy losses to be more stochastic. If the variation is smaller, then the energy loss should be more continuous. This leads to the hypothesis, that muon bundle events should have a smaller variation than neutrino muon events.

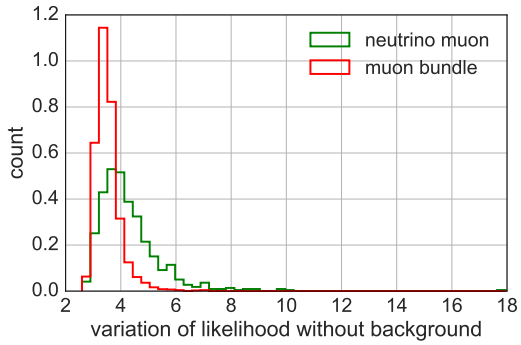

Figure 8.5: *Normed histograms of the variation of the signal likelihood for single muons and muon bundles*

The histogram in Figure 8.5 is an application of the variation defined above to the signal likelihood since I associate it with energy losses. The correlation between variation and

event type is as hypothesized. The correlation is not as clear as one would expect it to be if applied to the energy loss distribution since the likelihood function is smoothed due to scattering of photons.

	neutrino muons	atmospheric muons
Events kept	488	4561
Events sorted out	225	183

Table 8.4: *A table of the groups resulting from the criterion, that the variation of the signal likelihood be below 4.5*

Since the cuts discussed in this section are the focus of this chapter, they are harsher than the previous ones. In Table 8.4 the events sorted out are about half, but the error on atmospheric muons is also large compared to previous cut parameters with 183 out of 4561. The mean number of muons in the bundle for the sorted out events is 2.59, whereas it is 53.72 for kept events. This shows, that most sorted out events have a small muon bundle multiplicity.

Integral of absolute value

Here, the absolute Integral of the signal likelihood will be plotted for all remaining events. The total energy loss of a high energy muon is larger than that of several low energy muons with combined energy equaling the high energy one in the range of radiative energy losses (see Figure 3.11). Thus the integral over the likelihood, used as a measure for the total energy loss, should be smaller for muon bundle events.

The histograms in Figure 8.6 show the area under the raw likelihood for muon bundle and neutrino muon events. It is flatter for muon bundles than neutrino muons indicating some neutrino muons with higher energy loss rates than their bundle counterparts. Since the process of higher energy losses is stochastic it makes sense, that not all neutrino muons have consistently larger likelihoods.

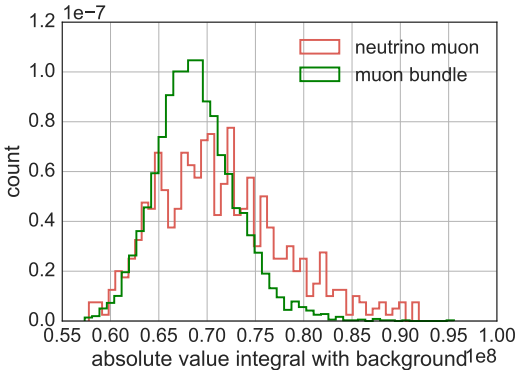

Figure 8.6: *Normed histograms of the absolute value Integral of the raw likelihood for single muons and muon bundles*

	neutrino muons	atmospheric muons
Events kept	369	4416
Events sorted out	119	145

Table 8.5: *A table of the groups resulting from the criterion, that the absolute value integral of the raw likelihood be below 40000*

The results of the cut placed on the integral is illustrated in Table 8.5. It is clear, that the total area under the likelihood curve is not the best parameter for differentiating between the two event types, but all parameters based on the likelihood function I have investigated are strongly related to either the absolute integral or the variation of it. Thus I will keep the absolute integral discussion. The main problem of the absolute integral parameter is, that the distribution of atmospheric muons is only flatter but does not vanish at some point. It follows that a fairly large error of 145 out of 4416 is made.

	neutrino muons	atmospheric muons
Total number of events	5645	4770
Events remaining after first characterization	713	4744
in percent	13 %	99 %
Events remaining after second characterization	369	4416
in percent	7 %	93 %

Table 8.6: *Table containing the results of the characterizations of muon events discussed*

The Table 8.6 summarizes everything discussed in this section. The conventional methods already used to differentiate between atmospheric muons and neutrino muons perform much better than the likelihood based parameters. With likelihood based cuts about a half of the neutrino muons can be sorted out at a cost of a 6 % error rate increase. If such a method were to be used, the relation between energy and likelihood has to be improved.

Another interesting investigation is the relation between these likelihood parameters and the number of muons in a bundle, but the reconstruction of the energy is currently not good enough to extract information about the number of muons from the parameters.

9 Conclusions

Since the PDF for the time residuals used in this entire analysis adequately filters photons from unrelated muon track segments, the results for the positions estimation of cascade vertices have been largely positive. The are problems with the position estimation. The background for the likelihood of low energy muons is far too large. So a cut on considered hits might be an option, such as changing the definition of a coincidence and just considering the first coincidence for any given DOM. The methods used for hit selection should be energy dependent since the quality of the reconstructed likelihood is so strongly energy dependent. The same method could help the cascade reconstruction of muon bundle tracks, which are also bad due to large background producing false positives.

Another improvement on the vertex position estimation might be made by also modulating the likelihood with the distance from the center of the detector and the direction of the particle to include an estimation on photons not registered by the detector.

The energy estimation is an even bigger problem, since the likelihood and the energy could not even be properly related up to a factor of ten. This is to be expected, since the likelihood does not consider the hit multiplicity. The first step at energy reconstruction would be to correlate coincident hits and likelihood at a given hypothesis for the energy reconstruction. An energy reconstruction as used in aashowerfit could work, but was not designed to reconstruct cascades. This energy reconstruction might be inappropriate since it uses the maximal distance, photons travel to estimate energy which is skewed since the muon is track like. All of this could be counteracted by placing a strong enough cut on time residuals, which also puts a cut on the maximum distance traveled due to the scattering length of photons in water. Having fewer photons, that travel far due to time residual cuts would skew the energy reconstruction.

The most appropriate energy estimation would most likely include the amount of light associated with the specific energy loss, the time residuals of the vertex hypothesis and the angle between DOM to vertex and particle direction. This work has shown, that the principle of first performing a scan along the track to perform a simple calculation of a likelihood using time residuals and then fitting energies to the found vertices might be a very good way to save computation time. This is compared to other energy reconstructions like millipede, that takes about two hours for an event and performs an energy estimation

at every vertex hypothesis.

The characterization of muon events is mainly based on the quality of the reconstruction. Properties of the likelihood function should be discussed again after some form of energy fit has been implemented.

Nomenclature

$\mathcal{P}$(k40)	Probability for K40 background to produce a hit
α	Spectral index
β_0	JGandalf quality parameter
β_1	JGandalf quality parameter
β_μ	Muon velocity in units of c
μ	Muon travel distance
ΔE_{MC}	Monte Carlo energy lost in the detector
λ_γ	Mean free path of pair production for a photon
λ_{e-}	Mean free bremsstrahlung path for an electron
$\mathcal{C}$	The set of all 4d coincident hits for an event
$\mathcal{H}$	Set of all hit PMTs for an event
$\mathcal{PDF}$	Probability density function
$\mathcal{U}$	Set of all unhit PMTs for an event
$\mu(E)$	mean number of photons detected for shower of energy E
τ	Time in four space
Θ	Angle between reconstructed track and MC track
θ_{ch}	Cherenkov angle
$\vec{D}_x$	x component of the reconstructed direction
$\vec{D}_y$	y component of the reconstructed direction
$\vec{D}_z$	z component of the reconstructed direction
$\vec{H}$	Direction hypothesis
$\vec{P}$	PMT direction
$\vec{P}_x$	x component of the reconstructed vertex
$\vec{P}_y$	y component of the reconstructed vertex
$\vec{P}_z$	z component of the reconstructed vertex

$\vec{v}_d$	Distance vector between DOM d and shower position
c_0	Speed of light in vacuum
c_m	Speed of light in medium
d_p	Photon travel distance
d_{mest}	Distance of the initial reconstructed vertex from the MC track
d_{peak}	Distance between first and second bang found by Belle Starr
E_{Gandalf}	Energy reconstructed by JGandalf
E_{MC}	Monte Carlo energy
E_{rec}	Reconstructed energy
h_t	Time of a hit h
h_{counts}	Number of hits for the coincidence hit after merging
h_{pos}	Position of a hit h
I_N	Cosmic ray intensity
L	Lateral spread of bundle muons
L	The Likelihood sum for all PMTs
L_{Gandalf}	Likelihood of the JGandalf reconstruction
L_{red}	JGandalf likelihood normalized by number of hits
m	Mass of particle
p_μ	Momentum four vector
p_t	Time of a scan point p
p_{pos}	Position of a scan point p
p_{shower}	Shower hypothesis position and time for a given event
q	Charge of particle
r_{event}	Minimal distance of the track from the detector center
t_μ	Muon travel time
t_p	Photon travel time
T_x	Direction cosine uncertainty in x direction
T_y	Direction cosine uncertainty in y direction
t_{res}	Time residual
v_μ	Muon velocity
X_0	Radiation length

X_{bundle}	Set of x positions of bundle muons
Y_{bundle}	Set of y positions of bundle muons
z_{event}	z coordinate of the likeliest energy loss reconstructed by Belle Starr
ARCA	**A**stroparticle **R**esearch with **C**osmics in the **A**byss
DOM	**D**igital **O**ptical **M**odule
h	4d hit containing time and space coordinates
hits	The set of all hits for an event
KM3NeT	Cubic Kilometre Neutrino Telescope
L0	Triggering level 0
L1	Triggering level 1
L2	Triggering level 2
LHC	**L**arge **H**adron **C**ollider
ORCA	**O**scillation **R**esearch with **C**osmics in the **A**byss
p	4d scan point containing time and space coordinates
PMT	**P**hoto **M**ultiplier **T**ube
UHECR	**U**ltra **H**igh **E**nergy **C**osmic **R**ays

Bibliography

[A. 14] A. Heijboer: *Shower Direction Reconstruction: aashowerfit.* KM3NeT Internal Note, 2014.

[Adr16] Adrian-Martinez, S. and others: *Letter of intent for KM3NeT 2.0.* J. Phys., G43(8):084001, 2016.

[BEH09] Blümer, J., R. Engel J. R. Hörandel: *Cosmic rays from the knee to the highest energies.* Progress in Particle and Nuclear Physics, 63:293–338, 2009.

[Car09] Carminati, G. and Bazzotti, M. and Biagi, S. and Cecchini, S. and Chiarusi, T. and Margiotta, A. and Sioli, M. and Spurio, M.: *MUPAGE: a fast atmospheric MUon GEnerator for neutrino telescopes based on PArametric formulas.* 2009.

[Dav02] David J.L Bailey: *Genhenv5r1 Software Documentation.* ANTARES-Soft/2002-004, 4 2002.

[Enb08] Enberg, Rikard and Reno, Mary Hall and Sarcevic, Ina: *Prompt neutrino fluxes from atmospheric charm.* Phys. Rev., D78:043005, 2008.

[GH02] Gaisser, T. K. M. Honda: *Flux of atmospheric neutrinos.* Ann. Rev. Nucl. Part. Sci., 52:153–199, 2002.

[Ham07] Hamamtsu Photonics K.K.: *Photomultiplier tubes: Basics and applications.* 3a , 2007.

[Ham15] Hamamtsu Photonics K.K.: *Photomultiplier tube*, 7 2015.

[Ing97] Ingelman, G. and Edin, A. and Rathsman, J.: *LEPTO 6.5: A Monte Carlo generator for deep inelastic lepton - nucleon scattering.* Comput. Phys. Commun., 101:108–134, 1997.

[Kat12] Katz, U. F. and Spiering, Ch.: *High-Energy Neutrino Astrophysics: Status and Perspectives.* Prog. Part. Nucl. Phys., 67:651–704, 2012.

[KBS01] Klimushin, S. I., E. V. Bugaev Igor A. Sokalski: *Precise parametrizations of muon energy losses in water. 27th International Cosmic Ray Conference (ICRC 2001) Hamburg, Germany, August 7-15, 2001*, 1009, 2001. [3,1009(2001)].

[Pat16] Patrignani, C.: *Review of Particle Physics.* Chin. Phys., C40(10):100001, 2016.

[Pen10] Peng J, Peng S, Jiang A, Wei J, Li C, Tan J: *Asymmetric least squares for multiple spectra baseline correction.* Anal Chim Acta, 683:63–8, 2010.

[Sch13] Schukraft, Anne: *A view of prompt atmospheric neutrinos with IceCube.* Nucl. Phys. Proc. Suppl., 237-238:266–268, 2013.

[Sch16] Schröder, Frank G.: *Radio detection of Cosmic-Ray Air Showers and High-Energy Neutrinos*. 2016.

Thanks

I would like to thank Clancy James for his suggestions and guidance. I also would like to thank Jacqueline Catalano, Judith Höfer, Laura Herold and Johannes Schäfer for proof reading my thesis.

Erklärung

Hiermit bestätige ich, dass ich diese Arbeit selbstständig und nur unter Verwendung der angegebenen Hilfsmittel angefertigt habe.

Erlangen, der 16. 12. 2016